

Mapping water vapour variability over a mountainous tropical island using InSAR and an atmospheric model for geodetic observations

Article

Accepted Version

Creative Commons: Attribution-Noncommercial-No Derivative Works 4.0

Webb, T. L., Wadge, G. and Pascal, K. (2020) Mapping water vapour variability over a mountainous tropical island using InSAR and an atmospheric model for geodetic observations. *Remote Sensing of Environment*, 237. 111560. ISSN 0034-4257 doi: <https://doi.org/10.1016/j.rse.2019.111560> Available at <https://centaur.reading.ac.uk/87723/>

It is advisable to refer to the publisher's version if you intend to cite from the work. See [Guidance on citing](#).

To link to this article DOI: <http://dx.doi.org/10.1016/j.rse.2019.111560>

Publisher: Elsevier

All outputs in CentAUR are protected by Intellectual Property Rights law, including copyright law. Copyright and IPR is retained by the creators or other copyright holders. Terms and conditions for use of this material are defined in the [End User Agreement](#).

www.reading.ac.uk/centaur

CentAUR

Central Archive at the University of Reading

Reading's research outputs online

1 **Mapping water vapour variability over a mountainous tropical island using InSAR and**
2 **an atmospheric model for geodetic observations**

3

4 T. L. Webb^{1,2}, G. Wadge¹, K. Pascal^{3,4}

5

6

7 1. Department of Meteorology, University of Reading, UK

8 2. Laboratoire d'Aérodynamique, Observatoire Midi-Pyrénées, Toulouse, France

9 3. Montserrat Volcano Observatory, Montserrat

10 4. Seismic Research Centre, University of the West Indies, Trinidad & Tobago

11

12

13 **Abstract**

14

15 The three dimensional distribution of water vapour around mountainous terrain can be highly
16 variable. This variability can in turn affect local meteorological processes and geodetic
17 techniques to measure ground surface motion. We demonstrate this general problem with the
18 specific issues of a small tropical island, Montserrat. Over a period of 17 days in December
19 2014 we made observations using InSAR and GPS techniques, together with concurrent
20 atmospheric models using the WRF code. Comparative studies of water vapour distribution and
21 its effect on refractivity were made at high spatial resolution (300 m) over short distances (~ 10
22 km). Our results show that model simulations of the observed differences in water vapour
23 distribution using WRF is insufficiently accurate. We suggest that better use could be made of
24 the knowledge and observations of local water vapour conditions at different scales, specifically
25 the Inter Tropical Convergence Zone (ITCZ), the trade wind fields and the mountain flow (~30

26 m) perhaps using eddy simulation. The annual perturbations of the ITCZ show that the range
27 of humidity is approximately the same expressed as the differential phase of InSAR imaging
28 (~100 mm). Trade wind direction and speed are particularly important at high wind speeds
29 driving vigorous asymmetrical convection over the island's mountains. We also show that the
30 slant angles of radar can follow distinct separate paths through the water vapour field. Our study
31 is novel in demonstrating how synoptic-scale features and climate can advise the modelling of
32 mesoscale systems and sub-seasonal InSAR imaging on tropical islands.

33

34 Keywords: water vapour, mountainous tropical island, ITCZ, InSAR

35

36 **1. Introduction**

37

38 Variation in the refractivity of the Earth's atmosphere can change the path and travel time of
39 radiation passing through it. Making use of this behaviour contributes to boundary-layer
40 meteorology (Stull, 1988), geodetic techniques such as Global Navigation Satellite Systems
41 GNSS (Hofmann-Wellenhof et al., 1995) and synthetic aperture radar interferometry (InSAR)
42 (Hanssen, 2001). Changes in refractivity are characterised by air temperature and pressure,
43 particularly the partial pressure of water vapour (Bevis et al., 1994). Water vapour content
44 generally increases downwards through the atmosphere and is most variable within the
45 atmospheric boundary layer (ABL), a few kilometres thick and is the dominant reservoir of
46 water vapour (Bengtsson, 2010).

47

48 Here we are mainly concerned with the varying refractivity of the atmosphere as it affects data
49 collected by the InSAR method in which two phase images of the scene of interest are acquired
50 at different times, but from very similar orbital positions, yielding coherent images of
51 differential phase “delay”. A common goal is to acquire the differential phase corresponding to
52 land surface motion, having systematically removed or minimised the other “noise” effects
53 (Hanssen, 2001). Of these effects, atmospheric water vapour variability has been the most
54 difficult to remove. This is because of its rapid decorrelation over length scales of ~ 100s of km
55 and time scales of ~ 10s of days that are typical of Low Earth Orbit (LEO) radars used for most
56 InSAR missions. Ways to mitigate the atmospheric noise have included independent
57 observations of water vapour (e.g. GNSS, Li et al., 2005); the use of statistical time series
58 methods with long datasets (e.g. Bekaert et al., 2015; Li et al., 2019) and models that simulate
59 the atmosphere at the time of radar imaging. (e.g. Jolivet et al., 2011, 2014). The latter is the
60 approach we use here, which is of considerable generality but difficult to apply in practice. For

61 example, the initial conditions for the model are hard to generate, and convection is difficult to
62 represent without using parameterizations. We do present other relevant data (e.g. GNSS and
63 radiosonde), but do not attempt to combine them with atmospheric modelling to find an optimal
64 joint solution. Montserrat is fortunate in having a dense network of GPS stations and a radiosonde
65 site at a distance of ~ 100 km. We use these two sources to generate water vapour variability
66 measurements to validate the numerical model- radar approach.

67

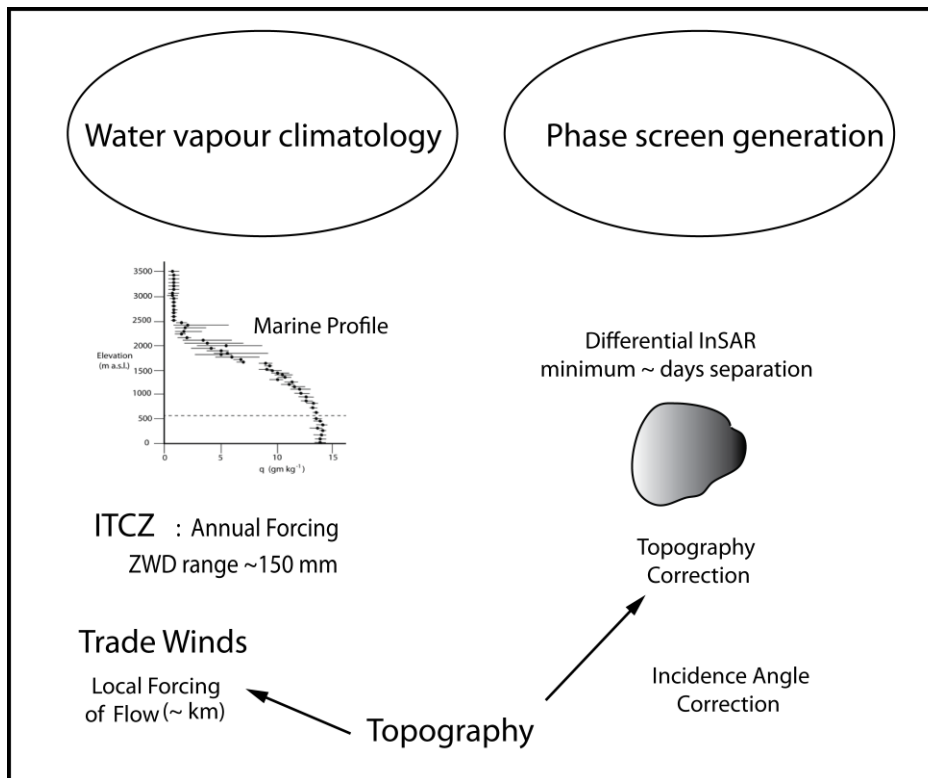
68 Conventionally for InSAR, the atmospheric contribution to the radar delay is considered to
69 comprise four major components: Wet Delay (WD, due to water vapour), Liquid Water Delay
70 (LWD), Hydrostatic Delay (HSD, due to atmospheric pressure) and Ionospheric Delay (due to
71 electron density in the area of the atmosphere affected by solar radiation), (Hanssen, 2001).
72 Recent studies (Feng et al., 2017) ; Fattahi et al., 2017), have shown that the ionospheric
73 contribution can be significant for low frequency radars (e.g. L-band, 1.27 GHz) studying large
74 length scales (several 100 km). For our scale of study, the magnitude of ionospheric phase
75 delay at a much higher frequency (X-band, 9.65 GHz) and a much smaller length scale (~ 10
76 km), are of much lower magnitude, allowing us to ignore that component. Hydrostatic delay
77 variation can be significant at times of large surface pressure change (Tregoning and Herring, 2006), in
78 areas of great topographic relief (~ 5 km, Elliott et al, 2008). We choose to ignore this effect in the case
79 of Montserrat.

80

81 Differential InSAR, in which phase difference images are created from pairs of radar images
82 separated in time, is sensitive to the changes in liquid water in clouds and particularly water
83 vapour content along the radar path over this time period. Differential InSAR is an increasingly
84 valuable tool for monitoring volcanoes (e.g. Lu and Dzurisin, 2014). Differential ground
85 motions of a few mm can be detected and modelled in terms of pressurized magma storage and
86 eruption processes (Pritchard et al., 2018; Ebmeier et al., 2018). However, many volcanoes

87 have substantial edifices (>1 km high) such that the radar path to the base of the volcano has to
88 pass through more water vapour than the equivalent path to the summit of the volcano. In this
89 way the phase difference can be strongly modulated by topography. The resulting pattern of
90 phase differences may be very similar to surface deformation generated by a pressure source
91 centred within or below the edifice. This potential confusion of signals has been the subject of
92 considerable study (e.g. Massonnet and Feigl, 1998; Wadge et al., 2002). This is particularly
93 relevant for volcanoes that have high relief and which generate complex patterns of airflow
94 associated with that relief. In these cases it is not just the topography that modulates the water
95 vapour field but the dynamic flow of air over and around it. Here we address these processes
96 using repeated InSAR measurements and numerical models of the delay due to atmospheric
97 water vapour content.

98
99 The physical and temporal scales of the radar results and the steep island terrain provides a set
100 of constraints distinct from equivalent continental scale studies ($\sim 10^5 - 10^4$ km²), that tend to
101 rely on the analysis of large radar datasets (e.g. Bekaert, et al., 2015, Alshawaf, et al., 2015).
102 This in turn gives us the opportunity to better understand small-scale ($\sim 10^3 - 10^2$ km²)
103 processes involving the distribution of water vapour. Our investigation is set in the humid
104 tropics. This has a distinctive climate driven by the Inter Tropical Convergence Zone (ITCZ)
105 (Schneider et al., 2014), the Low-Level Jet (Munoz et al., 2008) and their interrelationship
106 (Laderach and Raible, 2013) It is this combination of tropical climatology, diurnal boundary
107 layer dynamics and localised, steep topography that is clearly important but little studied and
108 forms the innovative basis of our study. Rather than relying on ever more difficult-to –
109 constrain initial conditions to the simulation of local delay fields, we propose that bringing to
110 bear climatological data and insights will enable improved models to be created .We
111 demonstrate this approach qualitatively in Fig. 1.



113

114 *Fig.1 Schematic illustration of the potential use of water vapour climatology to mitigate the effects of*
 115 *tropospheric phase delay water vapour variability. On the right is a set of standard processing measures*
 116 *in the use of differential InSAR, as used in this study. In contrast, on the left are three aspects of water*
 117 *vapour climatology discussed in the text. Note that, apart from topography, there is no treatment that*
 118 *links the two sets of measurements.*

119

120 The objectives of this study are to:

121

122 1.1 Understand where and when tropical water vapour originates.

123

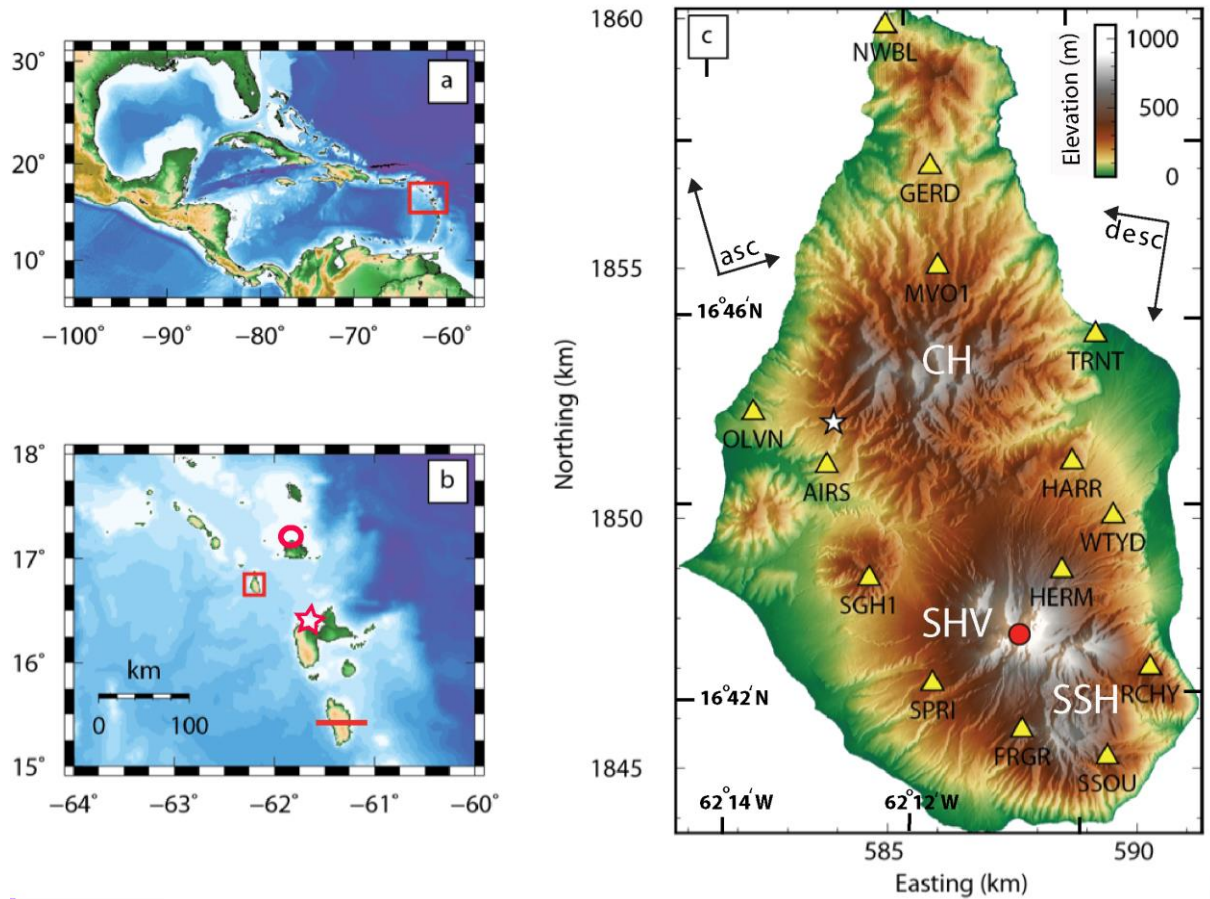
124 1.2 Measure and simulate the water vapour field over a small mountainous tropical volcano
 125 using InSAR phase fields, equivalent atmospheric models and GNSS (and local field data)
 126 during a 17-day campaign.

127

128 1.3 Show that the ambient state of the ITCZ, the trade winds and the radar viewing geometry
 129 can play important roles in the variability of water vapour.

130
131
132
133
134

These objectives provide the structural sub-headings used in the Discussion.



135
136
137
138
139
140
141
142
143
144
145
146
147

Fig.2 Location of Montserrat. (a) In the eastern Caribbean Sea (red box) , (b) In the central Lesser Antilles, framed by a red box. The red circle denotes the location of Antigua (Fig.4), the red star represents Le Raiset, Guadeloupe where sondes are launched (Fig. 12), and the red line represents the transect across Dominica for the model results shown in Fig.8).(c) Shaded elevation map of Montserrat (McVicar and Korner, 2013) showing the locations and names of the continuous GPS stations (yellow triangles). The white star gives the position of the Montserrat Volcano Observatory and the red circle is the lava dome of the Soufrière Hills Volcano (SHV). CH is the location of the Centre Hills, SSH is the South Soufrière Hills. ASC shows the orientation of the ascending pass satellite track and incidence azimuth. DESC shows the same for the descending pass satellite track. The internal coordinates are latitude and longitude, the external coordinates are the local grid for Montserrat.

148

149

150

151 **2. The Study Site: Montserrat, Lesser Antilles**

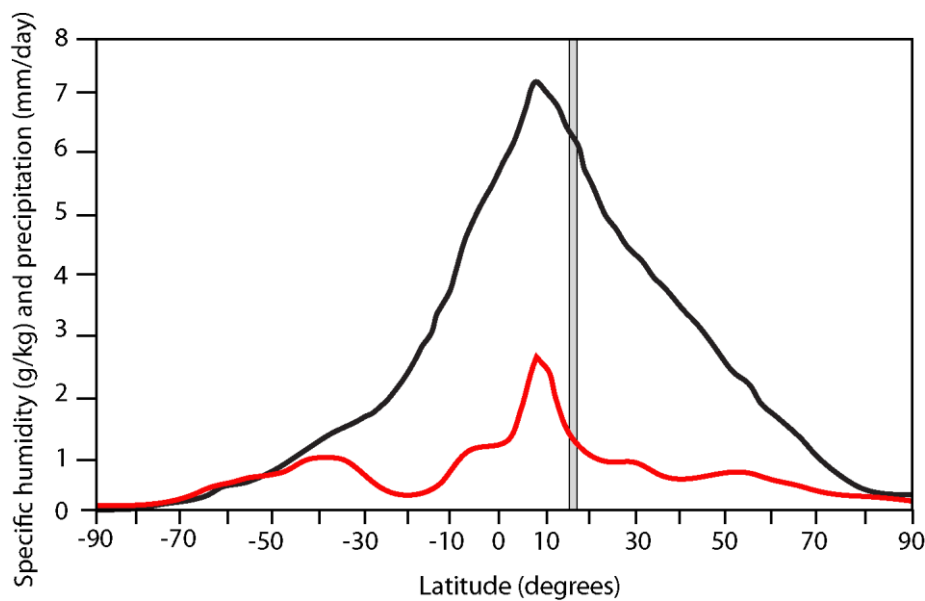
152

153 We base our study on Montserrat (Fig. 2), a small (~10 x 16 km) volcanic island in the Lesser
154 Antilles (17°N, 62°W). The Soufrière Hills Volcano (SHV), whose summit is about 1083 m
155 above sea level (a.s.l), occupies the southern half of the island, and has been active since 1995,
156 causing the destruction of the capital city Plymouth and the emigration of more than half the
157 population (Fig.2c) (Wadge et al., 2014). Improved geodetic monitoring is important for the
158 mitigation of future volcanic risk in Montserrat (Odbert et al., 2014) and at other similar
159 volcanoes.

160 The Lesser Antilles islands sit in the eastern Caribbean Sea a region of atmospheric interactions
161 that determine the humidity, winds and rainfall experienced (Taylor and Alfaro, 2005). The
162 main mechanisms involve the Atlantic, or western, part of the Inter Tropical Convergence Zone
163 (ITCZ) and the North Atlantic Subtropical High (NASH) (Waliser and Gautier, 1993; Martinez
164 et al., 2019). The ITCZ is a global zone of clouds and storms together with the trade winds
165 blowing from the east and from the east southeast at different times of year (Richter et al.,
166 2017). The NASH provides strongly divergent winds and atmospheric subsidence in the eastern
167 Caribbean atmosphere. As the ITCZ migrates northwards away from the equator in the boreal
168 summer, it reaches its most northerly position in June, July and August (JJA). Specific humidity
169 increases at the latitude of Montserrat, within a range of about 1- 6 g/kg (Fig.3). However, this
170 field is highly smoothed in Fig.3 and humidity varies strongly on a small scale in both space
171 and time (Bengtsson, 2010).

172 The ITCZ is particularly important because the evaporation flanking the ITCZ forms the main
173 baseline source of humidity for the Lesser Antilles. Figure 3 shows the zonal mean distribution
174 of observed specific humidity and precipitation based on ERA-interim reanalysis data
175 (Laderach and Raible, 2013) for July, the pivotal point of the migration. The ITCZ migration
176 from the equator during JJA also involves the strengthening of the southeast trade winds at
177 ground level, from 3.2 m/s in April to 5.4 m/s in July (Richter et al., 2017).

178

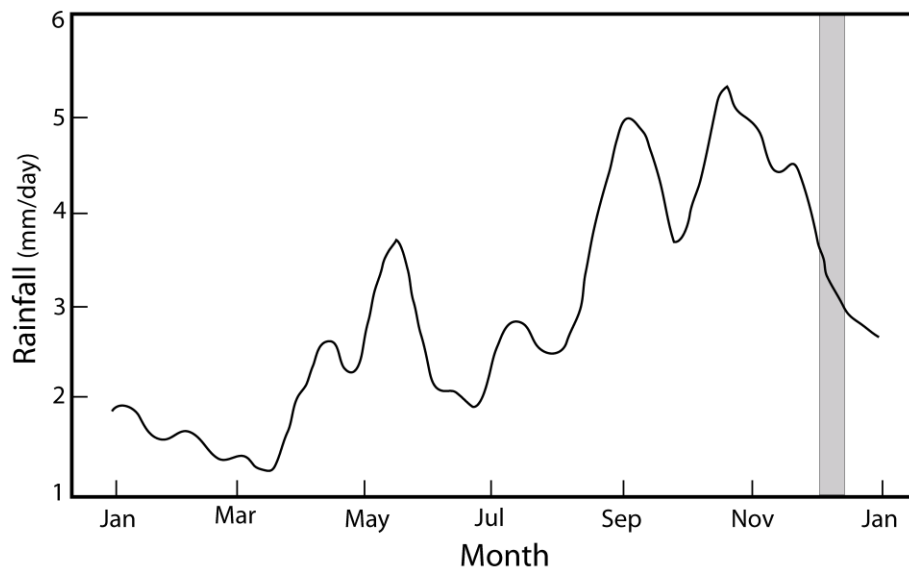


179

180 *Fig.3 Latitudinal plot of the zonal mean distribution of observed specific humidity and precipitation of*
181 *the ITCZ for July from 1979 to 2010. The black curve is from ERA-interim specific humidity data, the*
182 *red curve is for precipitation. The grey rectangle covers the location of the study site (after Laderach*
183 *and Raible, 2013).*

184

185 Figure 4 shows the annual impact that the ITCZ has on rainfall in the Lesser Antilles, in this
186 case in Antigua, to the northeast of Montserrat (Fig.2b). December to March is a dry season
187 followed by rising rates of rain with an irregular peak in November, a pattern common to many
188 islands in the Lesser Antilles. The difference in rainfall rate over the year due to the migration
189 of the ITCZ in the Eastern Caribbean is about 5 mm/day (Fig.4).

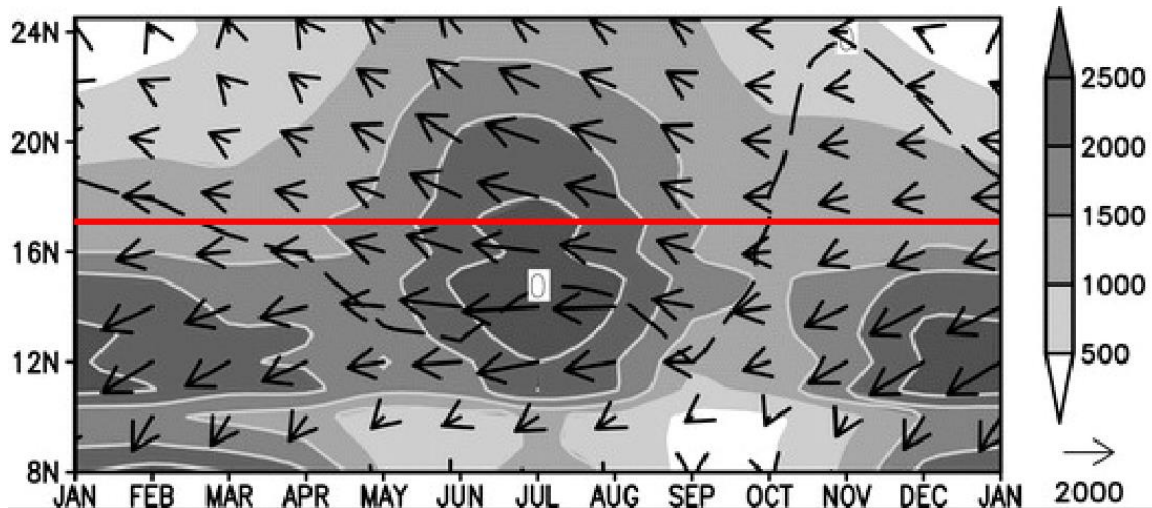


190

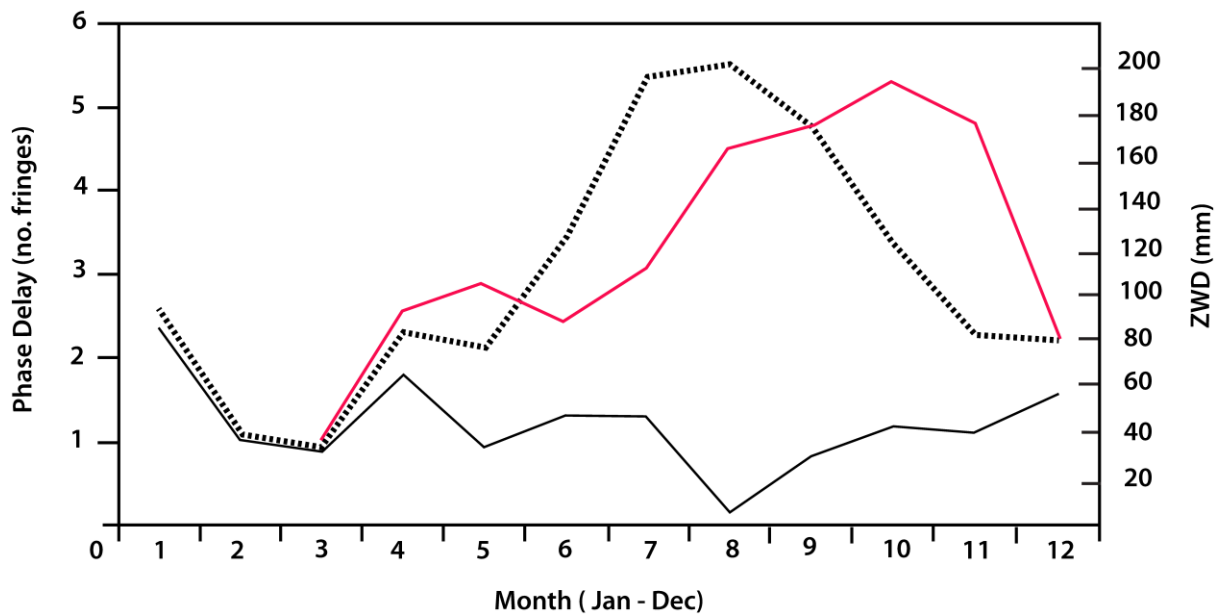
191 *Fig.4 Rainfall climatology for 1969-2017 at Antigua, northeast of Montserrat. Values are average*
 192 *rainfall in mm/day (adapted from Martinez et al., 2019). The grey band is the period of radar data*
 193 *acquisition in December 2014 that is studied in detail.*

194

195 Another significant feature of the tropical circulation are the low level jets (LLJs). These
 196 are regions of high winds in the lower troposphere coupled with an annual cycle of
 197 precipitation and a rainy season extending from May through October in the Caribbean
 198 (Munoz et al., 2008). There is a temporal maximum in wind speeds in July and a
 199 minimum in February (Fig.5). Spatial (zonal) wind speed maxima occur at a pressure of
 200 about
 201 925 hPa (~700 m above sea level) with speeds reaching maxima of ~ 14 ms⁻¹ in July
 202 and minima of ~8 ms⁻¹ in October (Fig.5). Diurnal wind speed variability tends to peak
 203 in the
 204 morning.



212
 213 Fig. 5 The zonal moisture flux across the Caribbean plotted in latitudinal-monthly space. The grey
 214 shading is of moisture flux and the arrows are moisture flux vectors generated from the North American
 215 Regional Reanalysis (NARR, Munoz et al., 2006). Montserrat's location is represented by 17N latitude
 216 (solid red line) and by December. The moisture flux decreases about a peak value in July of $2500 \text{ g kg}^{-1} \text{ m s}^{-1}$
 217 to about half that between October and April.



218
 219 Fig.6 Plot of monthly mean phase delays at Fogo volcano between June 2005 and December 2007
 220 (Black dashed line gives the number of delay fringes, black continuous line gives the standard deviation)
 221 (adapted from Heleno et al., 2010). Red line gives an equivalent plot of monthly phase ZWD delays
 222 averaged from March 1998 to November 2000 at SHV volcano on Montserrat (taken from Wadge et al.,
 223 2006).

224 In the eastern Atlantic part of the ITCZ, the Fogo Volcano shows a similar behaviour to that at
225 SHV, Montserrat (Heleno et al., 2010). Using a 2.5 year-long dataset of 71 ASAR radar images
226 Heleno et al. were able to show strong seasonal signals of humidity and resulting phase delay
227 (Fig.6). The amplitude of the ITCZ-derived annual variability of water vapour at Fogo was
228 measured at up to 17 cm of equivalent ground motion between sea level and about 2000 m a.s.l.
229 (Fig.6). This agrees with independent MODIS-derived, precipitable water vapour (PWV)
230 values. Montserrat has a similar annual relationship to Fogo in this regard. Fig.6 shows the
231 monthly ZWD variation values over a 2.5-year period. Whilst the SHV and Fogo have slightly
232 different peaks in their water vapour contents the broad pattern of dominant water vapour
233 content in the winter is obvious. Effectively, much of the seasonal water vapour signal
234 variability is generated by the ITCZ migration. From the perspective of InSAR geodetic
235 monitoring, the variability of differential phase will tend to be much greater if the
236 interferometric pair comprises data from, say, May and November, rather than from January to
237 April (Fig.6).

238 The strength and timing of the ITCZ varies from season to season and from one year to the
239 next. For example, the wind direction data collected by Wadge et al., (2006) on Montserrat
240 between 1998 and 2000 (Table 5) shows monotonous easterly winds in April and highly
241 variable winds in July.

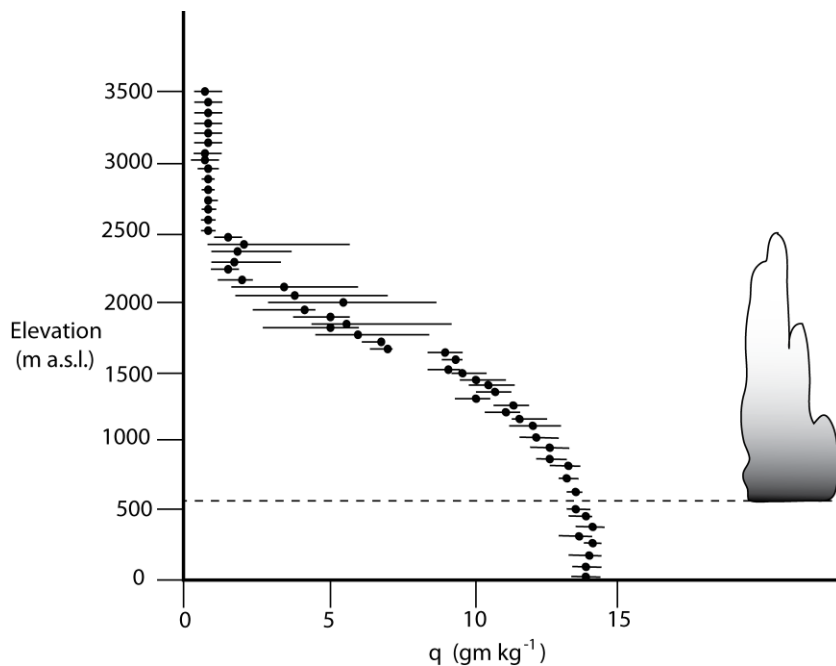
242
243 In addition to the ITCZ, weather systems at the 100-1000 km scale affect Montserrat. These
244 include cyclonic systems, up to hurricane strength, carried westward across the Atlantic as
245 “easterly waves” during the wet season, together with locally originating large convective
246 systems (Matthews et al., 2002; Barclay et al., 2006). Troughs of dry upper tropospheric air
247 also occur in the eastern Caribbean (e.g. Wadge et al., 2016). From our perspective the most
248 significant impact that these events have is their disruption of the ABL, particularly the speed
249 and direction of the wind over the island.

250 The ABL over the sea surrounding Montserrat is relatively simple compared to that over the
251 islands. The Atlantic Ocean ABL upwind from Montserrat was studied by the Barbados
252 Oceanographic Meteorological Experiment (BOMEX), (Siebsma et al., 2003) and the Rain in
253 Cumulus Over the Ocean (RICO), (Davison et al., 2013) field measurement campaigns.
254 Typically, cumulus cloud develops over the sea during the day, usually below a temperature
255 inversion. These clouds and other sub-cloud, high-moisture content air parcels act as triggers
256 for buoyant convection when advected over land (Kirshbaum and Smith, 2009) resulting in
257 taller and broader cumulus clouds over the islands. The water vapour field over the open ocean,
258 measured in the RICO study, typically takes the form of the profile shown in Fig.7 (Stevens,
259 2006). Below the lifting condensation level (LCL) the water vapour specific humidity is fairly
260 constant and reaches the highest values. Above it, within the cloud layer, the mean specific
261 humidity decreases strongly with altitude but its variability increases (Fig.7). Above the
262 cumulus layer the humidity often has a low, uniform value. Typically, the ABL has a thickness
263 of about 2 km but it can be up to 4 km in the winter months (Davison et al., 2013). Radiosonde-
264 derived specific humidity profiles for the days of radar imaging are discussed in section 5.1. A
265 strong diurnal cycle of water vapour variability was observed on 4-5 August, 2013 in the ground
266 radar interferometer measurements of Wadge et al. (2016) over Montserrat. The windward
267 slopes of the mountains were heated first at sunrise and a rapidly mixing layer driven by
268 convective heating developed over about 2 hours. This reached its maximum development in
269 the early afternoon. After sunset the ABL rapidly evolved to a much weaker mixed layer above
270 a lowermost stable layer, with greatly reduced variance in water vapour.

271

272 The trade winds in the Lesser Antilles mainly blow from east northeast. The relatively uniform
273 marine ABL changes its structure due to the interaction with topography and the daytime
274 heating of the islands' surfaces. The trade winds blow roughly perpendicular to the topographic

275 axes of the islands in the northern and central part of the arc such as at Montserrat, giving
276 asymmetrical windward and leeward characteristics. The
277 speed and direction of the trade winds play important roles in the development of clouds,
278 precipitation and topographic flows. The atmospheric processes over some of the islands of the
279 Lesser Antilles have been studied intensively in recent years. These include: cloud trails
280 forming due
281



282
283
284 *Fig.7 Profile of water vapour specific humidity (q) values measured during the 10th research flight of*
285 *the RICO campaign (Stevens, 2006). Above the LCL (dashed line, ~600 m a.s.l.) mean values of q (black*
286 *dots) decrease up to the top of the cumulus layer at about 2200 m a.s.l. (shown schematically on the*
287 *right), whilst the variability increases (black lines are the interquartile ranges).*

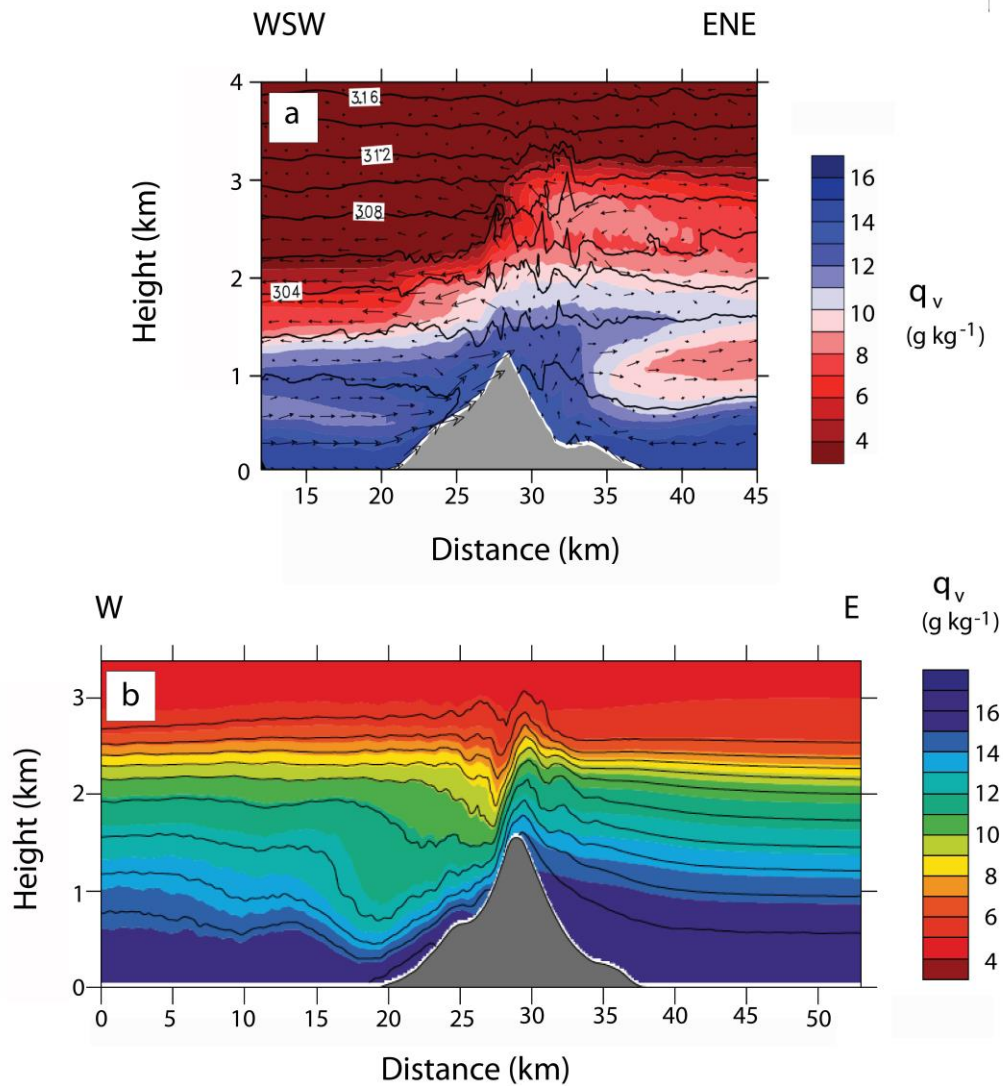
288
289 to diurnal heating (Smith et al., 1997; Kirshbaum and Fairman, 2015), island-induced winds,
290 including katabatic flow (Cécé et al., 2014), orographic precipitation (Kirshbaum and Durran,
291 2004; Kirshbaum and Smith, 2009; Smith et al., 2012), orographic convection (Minder et al.,

292 2013; Nugent et al., 2014; Wang and Kirshbaum, 2015) and volcanically-triggered rainfall
293 (Poulidis et al., 2016).

294 Dominica (200 km to the southeast of Montserrat) experiences similar trade wind weather to
295 Montserrat, and as shown in Fig.8a. For low wind speeds (<5 m/s) diurnal thermal convection
296 dominates (Smith et al., 2012), and the eastern (windward) side of the island in the case of low
297 wind speeds from the north, the eastern side of the island has a much more complex humidity
298 field than the western (lee)side. For high wind speeds (>7 m/s, Fig.8b) mechanically driven
299 convection occurs, most strongly over the eastern windward slopes, and the form of the
300 resultant water vapour field is reversed, with drier air above the leeward slopes. On Dominica,
301 Minder et al. (2013) showed that at high wind speeds (~ 12 m/s), plunging flow on the leeward
302 (western) slopes of the mountain reduces the specific humidity, at altitudes below about 1-1.5
303 km a.s.l. and around the summit, by up to 3-4 g/kg relative to values on the windward (eastern)
304 side.

305

306



307

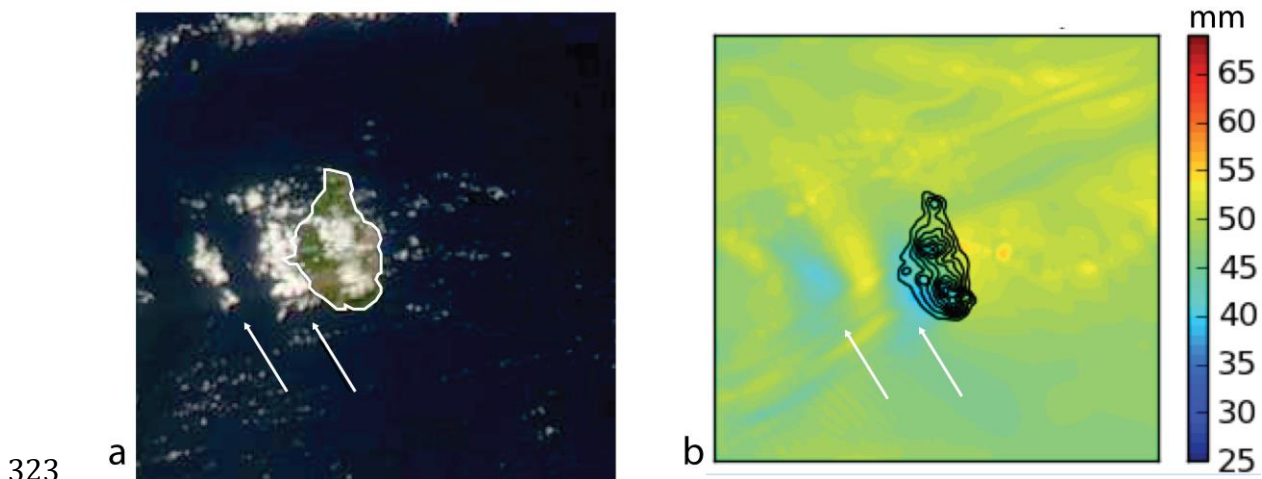
308 *Fig.8* Transects of modelled specific humidity fields from Dominica whose locations are
 309 approximately shown in Fig.2b. (a) Low wind speed WRF model with an ENE-WSW section output of a
 310 4-hr averaged water vapour specific humidity field (q_v , coloured) over Dominica. The wind direction is
 311 shown by arrows and the speed is low, about 2 m/s, from the north. Potential temperatures are given by
 312 the black lines. Data courtesy of D. Kirshbaum, from the study of Wang and Kirshbaum (2015). (b) High
 313 wind speed WRF model with an E-W section output of 6-hr averaged water vapour specific humidity
 314 field (coloured) over Dominica. The trade winds blow from the right (east-south-east) at a speed of
 315 about 12 m/s (from Minder et al., 2013).

316

317 Sometimes a train of lee waves will develop. Figure 9a shows an example of this captured by
 318 MODIS imagery of Montserrat at 17:30 local time on 3rd August 2013. A WMM image of

319 integrated water vapour content for the same time (Fig.9b) simulates well the two strong waves
320 that developed to the lee side of the island. The lee waves have peak-to-trough amplitudes of
321 about 15 mm of ZWD.

322



325

325 *Fig. 9 Lee waves produced downwind of Montserrat during trade wind flow at 17:30 on 3rd August*
326 *2013. (a) MODIS Terra image showing Montserrat (16 km N-S), outlined in white, covered in green*
327 *vegetation and buff volcanic deposits. Three banks of cumulus cloud produced by lee waves (white*
328 *arrows) are evident. (b) WMM simulation, at same time as (a), of the vertically integrated water vapour*
329 *content. See Fig.S1 for GPS-ZWD calculation.*

330

331 3. Methods

332 3.1 InSAR

333 A radar image of the ground surface, when compared to a geometrically equivalent image
334 acquired at another time can give a coherent measure of the phase change during that interval.
335 This is the principle of InSAR and, as in our case, the interferograms are acquired every few
336 days by radar-hosting satellites in sun-synchronous dawn-dusk orbits (Hanssen, 2011), using
337 GAMMA software. We requested from the Italian Space Agency (ASI) an intensive
338 observation campaign using the COSMO-SkyMed constellation of four X-band radars between

339 2 and 19 December 2014 (2,3,6,10,14,18,19 December). We made meteorological observations
 340 on the ground in Montserrat during the satellite imaging. The measured phase in the
 341 interferograms is the combined sum of components derived from the orbit (Fattahi and
 342 Amelung, 2014), the viewing geometry (Goldstein and Werner, 1998), the topography (Spaans
 343 and Hooper, 2016), the motion of the ground, the refractive delay of the atmosphere (Li et al.,
 344 2019), the nature of the surface scattering and noise (Zebker and Villasenor, 1992). In our case
 345 we can explicitly correct for the geometry from knowledge of the satellites' orbits and for the
 346 topography by using a 25m-DEM. GPS measurements made by MVO, show that there was no
 347 significant ground deformation during our survey (Stinton et al., 2016). The residual signal
 348 should be that due to the change in refractivity and noise, including uncompensated ground
 349 surface change.

350

351 *Table 1. COSMO-SkyMed imaging times and angles*

Date	Pass	Image Time (local time) ³	Sunrise/Sunset (local time)	Incidence Angle ¹ (°)	Azimuth Angle ² (°)
2/Dec/2014	asc	05:58	06:20	26.6	069
3/Dec/2014	asc	05:58	06:21	26.6	069
6/Dec/2014	des	17:34	17:35	59.2	281
10/Dec/2014	des	17:34	17:37	59.2	281
14/Dec/2014	des	17:34	17:38	59.2	281
18/Dec/2014	asc	05:58	06:29	26.6	069
19/Dec/2014	asc	05:58	06:30	26.6	069

352 1. Angle from vertical of radar impinging on surface.

353 2. Direction of look of radar in the horizontal plane (0-360° N=0, clockwise).

354 3. Local time is UTC - 4 hr.

355

356

357 *Table 2. Meteorological conditions at radar overpass*

Date	T (°C)	RH (%)	WV Lapse Mm/m	Wind RS ¹ (°) /m/s	Wind G ² (°) /m/s	Wind TR ³ (°) /m/s
2/Dec/2014	24	89	0.075	087/5	070/2	175/1
3/Dec/2014	24	89	0.107	040/3	030/11	140/2
6/Dec/2014 ⁴	23	90	0.097	258/5	330/7	190/2
10/Dec/2014 ⁵	25	80	0.098	148/6	170/3	100/2
14/Dec/2014	25	70	0.098	135/9	170/3	100/2
18/Dec/2014	23	83	0.095	009/1	070/2	000/2
19/Dec/2014	24	78	0.083	084/10	110/6	-

358 T = temperature, RH = relative humidity, WV lapse = water vapour content lapse rate

359 1. Wind velocity measured by radiosonde above Guadeloupe (<600m asl).

360 2. Wind velocity measured by anemometer at Gerald's airport.

361 3. Wind velocity measured at Tar River GPS site.

362 4. Mesoscale cumulus to southeast.

363 5. Cloud trails SSE to NNW (Kirshbaum and Fairman, 2015).

364

365 Table 1 gives details of the radar image acquisitions and table 2 gives the meteorological
366 conditions at the times of acquisition.

367 Random changes in time in the location or strength of the local scatterers within a radar beam
368 will increase the phase noise. Surfaces covered by wind-blown trees or rapidly growing
369 vegetation can become incoherent, whilst the phase signal from a rocky or soil-covered surface
370 may remain coherent. On Montserrat, the forests (at South Soufrière Hills and Centre Hills,
371 Fig.2c) become incoherent to X-band radar signals over a few hours. Because the phase
372 gathered by InSAR systems is modulo 2π , the ambiguity this creates must be removed by
373 unwrapping of the phase signal. Here we use a minimum cost flow method (Costantini, 1998).
374 Areas with incoherent signal or poor unwrapping of phase are masked. The ascending and
375 descending pass masks are different in detail, reflecting their viewing geometries, but largely

376 comprise the areas of Centre Hills and South Soufriere Hills (Fig.2c), which were not denuded
377 of forest cover during the 1995 - 2010 eruption.

378

379 3.2 Atmospheric Models

380 The small size of Montserrat requires a high-resolution model to represent both the topography
381 and its impact on airflow over and around it. The model used is the WRF Montserrat Model
382 (WMM) and a detailed description of the WMM can be found in Webb (2015). Céce et al.,
383 (2014) used a similar, though coarser, WRF-based model to represent Guadeloupe. The WMM
384 uses the European Centre for Medium-range Weather Forecasting, (ECMWF) operational
385 forecast data on a 16 km grid truncated onto a horizontal 19 km grid level as its initial condition,
386 and simulations are successively nested through domains with 8.1 km, 2.7 km, 0.9 km and 0.3
387 km grids. The lower domain boundary is a 30 s regional terrain dataset imposed on all nested
388 grids, except the 0.3 km grid, whose surface is represented by a bespoke mapping of the cover
389 of Montserrat by water, farmland, forest and bare rock. The topography is represented by a 25
390 m horizontal resolution DEM. Table 3 shows the parameterizations used in the WMM at each
391 domain level. In the vertical, the grid comprised 51 eta levels (using a terrain-following
392 hydrostatic pressure coordinate) skewed to the lower troposphere – the lowest region of the
393 atmosphere. A few closely packed layers near the upper domain boundary (20 km) were used
394 to control wave reflections. Adaptive time stepping was used (see table 3) and controlled by the
395 stability of the Courant-Friedrichs-Lewy condition on the innermost domain. The model spin-
396 up time was 10 hours.

397

398

399

400

401 *Table 3. Parameterisation options for WMM in each spatial domain*

	Domain 1	Domain 2	Domain 3	Domain 4
Resolution (km)	8.1	2.7	0.9	0.3
Starting Ts^{-1}	10	8	6	4
i start offset ²	1	65	65	52
j start offset ³	1	65	62	62
Cumulus	Grell Devenyi	Grell Devenyi	None ⁴	None ⁴

402 For each of the following parameters the values are common to all domains: Grid size (km), vertical levels (50,
 403 Planetary Boundary Layer = Yonsei, Radiation = Dudhia RRTM, Microphysics = Ferrier,
 404 Cumulus physics calls (min.) = 8, PBL physics calls = 8.

405 ¹Timestep used at start of a model run before adaptation by the CFL condition.

406 ²Grid offset from previous domain, units determined by outer domain.

407 ³No cumulus parameterisation needed at this domain resolution.

408 ⁴A call time of 0 means at every time-step.

409

410 From the WMM results we calculate the two-way travel zenith path delays for each day of the
 411 2,3,6,10,14,18,19 December dataset. We also differenced (earlier-later) the pairs of slant wet
 412 delay (SWD) fields from the WMM models corresponding to COSMO-SkyMed interferograms
 413 and then subtracted the WMM SWD fields from the interferograms. Identical fields would,
 414 assuming no other processes introducing signals, result in a perfect compensation for the
 415 observed water vapour delay and leave a uniform phase field.

416

417 3.3 GPS

418 MVO operates a network of 14 continuous GPS stations across Montserrat (Fig.2c). The data
 419 are telemetered to MVO and processed using GAMIT/GLOBK software (Herring et al, 2010 a,
 420 b). At any given interval there is a varying subset of the full GPS satellite constellation visible
 421 to each GPS site. The angle of elevation above the horizon of each satellite is variable. A

422 threshold elevation angle of 10° was used to reduce the noise from low-angled paths (Fig.10).
423 The refractive delay of the signal is greater for a satellite-GPS station path with a low elevation
424 angle. An estimate of the Zenith Total Delay (ZTD) (Herring et al., 2010) , was made using the
425 GAMIT/GLOBK processing suite incorporate the GPT2 model (Lager et al., 2013), which
426 combines the Global Pressure and Temperature (GPT) and Global Mapping Function (GMF)
427 empirical models, increasing their spatial (5° vs 20° grid) and temporal resolutions (annual and
428 semi-annual vs annual variations only), and provides daily a priori values of pressure,
429 temperature, water vapor pressures, and mapping function coefficients with a sampling rate of
430 30 s corresponding to the GNSS observations sampling rate. To further improve the accuracy
431 of the a priori temperature and pressure values at each GNSS stations, specifically at the time
432 of InSAR image acquisition (5h58 and 17h34 East Caribbean Time), we extract them from the
433 global climatic model NCEP. A comparison of the ZHD values computed using temperatures
434 and pressures from the GPT2 and the NCEF model shows an improvement of up to ~ 100 mm.
435 The ZWD (in mm of phase delay) equivalence to the water vapour amount (in mm of
436 precipitable water) is about 7 mm of phase delay to 1 mm of water. The values of ZWD are
437 calculated every hour using a piecewise linear function.

438

439 The accuracy of the ZWD estimate depends on the location of the satellites. The measurement
440 space for each GPS site is an inverted cone (Fig.10a). The GPS stations are well distributed
441 across the island, with nearest neighbour spacing of ~ 3 km (Fig. 2c). Stations on or near the
442 coast will have substantial parts of their measurement space over the sea. Depending on the
443 paths, this could lower the variability of the estimates if the marine troposphere is more uniform
444 than the island troposphere.

445 The elevation range of the GPS network covers only about half the vertical range of the island's
446 topography (12 to 589 m a.s.l. compared to 0 to 1083 m a.s.l.). Steep topography may cause the

447 line of sight of GPS to become blocked (Fig.10). With increasing elevation of the GPS site, the
448 measured ZWD value will tend to fall. The lapse rate of ZWD is measured by linear regression
449 of the 14 individual station values up to 589 m a.s.l.. This is justifiable if the water vapour
450 profile is near uniform over this elevation interval, as it is for example up to the LCL in Fig.7.
451 In the following we assume linearity of the lapse rate up to 1083 m a.s.l. The measured
452 departures from linearity are assumed to be caused by horizontal differences in water vapour
453 delay due to airflow. We wish to capture these lateral variations in ZWD and also vertical
454 modulation of ZWD due to topographic intersection with the water vapour field. A method to
455 achieve this is described in Supplement 1.

456

457 **4. Surface Topography and Wind**

458

459 The characteristics of the surface of Montserrat and the COSMO-SkyMed InSAR system
460 (Table.1) place limitations on the satellite observations of water vapour delay.

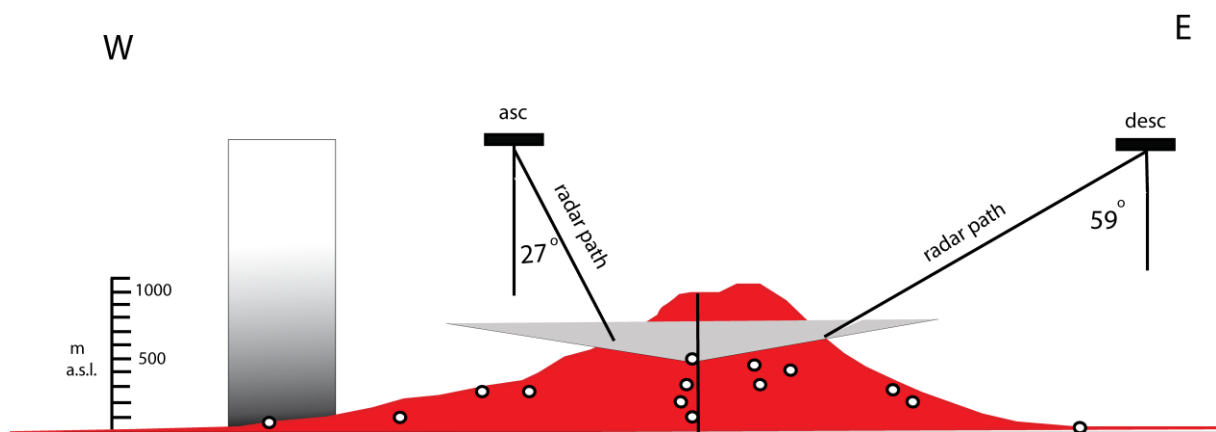
461

462 **4.1 Viewing Interval and Geometry**

463 The minimum interval between InSAR imaging using the same orbital geometry is about 12-
464 24 days (Pritchard et al., 2018). COSMO SkyMed has a constellation of four satellites and so
465 more frequent revisits were achieved on Montserrat: at intervals of 1- and 4-days. We used
466 seven images (of sufficiently high quality) here, on 2, 3, 6, 10, 14, 18 and 19 December 2014.
467 Two other images were supplied but were too decorrelated to form good quality interferograms.
468 The imaging paths of the COSMO-SkyMed radar are far from vertical and both the resultant
469 slant paths through the troposphere must be simulated in the WMM to give the slant wet delay
470 (SWD). The ascending pass images look at the surface more steeply (26.6° from vertical) than
471 the descending pass images (59.2° from vertical) (Figs.2c, 11). Thus, the radar paths through

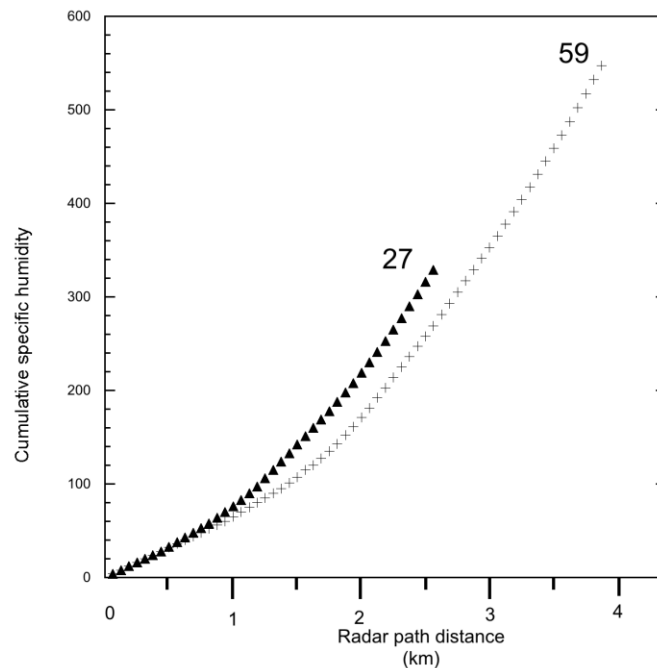
472 the ABL are longer for descending passes than for ascending passes. This would have no effect
 473 if the 3D water vapour fields were identical at the times of the two images forming the
 474 interferogram. But generally, temporally separated water vapour fields do vary spatially (e.g.
 475 Minder et al. 2013), so that we would expect the longer paths of the descending pass
 476 interferograms to create more spatial variance in the resulting delay fields. The mountain axis
 477 of Montserrat is oriented about 350° , roughly perpendicular to the usual easterly trade wind
 478 direction. This is also perpendicular to the azimuth of the radar look direction in the ascending
 479 pass but about 20° off the perpendicular for the descending pass (Fig.2c). Water vapour-derived
 480 variability should increase in descending pass interferograms as the radar path becomes more
 481 oblique to the mountain axis of the island and a longer path over the land surface with its high
 482 variability of water vapour. So, from both these geometrical effects we would expect the
 483 descending pass interferograms to show a greater amplitude of phase variance than for the
 484 ascending pass ones, other factors being equal.

485



486
 487
 488 *Fig.10 True scale cross section (W-E) through Montserrat at SHV (the location shown in Fig.2c). The ascending*
 489 *(27 degrees from vertical) and descending (59 degrees from vertical) radar slant paths are shown schematically.*
 490 *On the western side of the section is a gradational column schematically intersected by the surface of the SHV*
 491 *volcano. This is shown to emphasize the nature of the problem if the water vapour field is simply layered and the*
 492 *difference between the two can be captured by comparing two static layered fields. The MVO GPS receivers are*

493 shown as black circles plotted in the location of their projection on the section (see Fig.2c for their location in the
 494 x,y-plane). Note that there are no receivers above ~ 600 m a.s.l.. The grey triangle represents the apex of the
 495 sampling cone forming an angle of 10 degrees above the horizontal for one of the GPS receivers.
 496
 497



498
 499
 500 *Fig.11 Plot of the cumulative amount of specific humidity water vapour against radar path distance. The origin*
 501 *of the plot lies at a location about 3.5 km above the ground surface. The two curves (labelled 27 and 59) correspond*
 502 *to ascending and descending path satellites respectively, as shown in Fig.10. The two curves are similar until*
 503 *about 800 m when they start to diverge, the ascending path radar encountering water vapour faster until about*
 504 *2.5 km when it reflects from the ground surface. The descending path radar continues for just over another*
 505 *kilometre until it too hits the surface. The “59” radar records about 1.66 more water vapour than the “27” radar.*
 506

507 **4.2 Wind Speed**

508 The speed of the wind has been shown to affect the dynamics of orographic convection in
 509 several studies of the atmosphere around the mountains of the Lesser Antilles (Smith et al.
 510 2012; Minder et al., 2013; Cécé et al., 2014). The orientation of convection is highly

511 asymmetric (Nugent et al., 2014). At low wind speeds (<5 m/s) solar surface heating drives
512 convection with surface convergence forming clouds that are slowly moved downstream by the
513 mean wind (Fig.8a). At high wind speeds (>7 m/s) air is forced upward on the windward side
514 forming clouds and high humidity there, whilst to leeward there is plunging flow, reduced cloud
515 formation due to evaporation and reduced water vapour (Fig.8b). We measured the wind
516 velocities during the satellite overpasses (Table 2) from the ground surface near sea level, from
517 an airport anemometer close to the ground surface at about 160 m a.s.l. and from radiosonde
518 observations above Guadeloupe, about 100 km SSE of Montserrat. Following Nugent et al.
519 (2014) we use the average wind in the lower ABL (< 600 m a.s.l.) to determine the tripartite
520 classification of low, medium and high wind speeds. Wind speeds were “low” on 3 and 18
521 December, “high” on 14 and 19 December and “medium” for the other three days (Table 5) .
522 The wind direction was from east to west for six of the observation days, but with considerable
523 scatter. The wind direction changed from west to east on 6 December during the passage of a
524 low-pressure system to the southeast of Montserrat.

525 Wadge et al., (2006) collected wind speeds and strength at the time of acquisition of ERS C-
526 band radar images during 1998 – 2000 (Table 4). These show that the eastern quadrant
527 dominated the wind directions and strengths on Montserrat.

528
529
530

531 *Table 4. Wind speed by quadrant at the time of acquisition of ERS C-band images (between March 1998 –*
532 *November 2000) over the SHV on Montserrat (data from Wadge et al., 2006).*

Wind speed (m/s)	North	East	South	West
Low (< 5)	3	1	1	1
Medium (5-7)	1	6	0	0
High (>7)	2	13	2	0

533

534 *Table 5. Wind observations at the times of imaging in Dec. 2014.*

Date	Wind strength	Wind Direction	View/Time ²
02/Dec/2014	M	East	A
03/Dec/2014	L	East	A
06/Dec/2014	M	West	D
10/Dec/2014	M	Southeast	D
14/Dec/2014	H	Southeast	D
18/Dec/2014	L	East	A
19/Dec/2014	H	East	A

535 1. H=high ($> 7 \text{ ms}^{-1}$), M=moderate ($7\text{-}5 \text{ ms}^{-1}$), L =low ($< 5 \text{ ms}^{-1}$)

536 2. A=ascending pass/sunrise, D=descending pass/sunset

537

538 The above evidence shows that strong, easterly winds are most likely to develop strongly
539 asymmetrical convection patterns. We use data from the example of a strong, easterly wind on
540 Dominica modelled by WRF (Minder et al., 2013) shown in Fig.8 which we take to be
541 representative of behaviour at Montserrat. Using the geometry of the east-looking (23°)
542 ascending radar data and the west-looking (59°) descending pass data we find that the water
543 vapour fields detected by the descending pass radar are 1.66 greater than the ascending pass
544 case (Fig.11). It may be possible to extract some simplified states from this asymmetrical
545 behaviour that can be quickly used to predict a 3D water vapour field using ICTZ, trade wind
546 and precipitation, without using a full numerical weather prediction approach.

547

548 4.3 Diurnal Cycle

549 The potential effect of the diurnal cycle on radar refractivity is two-fold. Firstly, the state of the
550 ABL over the island encountered by the radar will depend on the timing of the satellite overpass

551 relative to the cycle (Table 1). In the case of the COSMO-SkyMed data we use, the ascending
552 overpasses of the satellite were at 05:58 local time, just before sunrise at 06:20, at what should
553 be a time of low refractivity noise (Wadge et al., 2016). The descending overpasses were at
554 about 17:34 local time, close to sunset at 17:35, again a time of expected low refractivity noise.
555 On the other hand WRF simulations of sunrise temperatures (e.g. Gonzalez et al., 2013) can
556 show abrupt inflections and noisier behaviour. Secondly, a satellite with an overpass later in
557 the morning, say, could be sampling a much more turbulent ABL than earlier in the cycle after
558 thermal convection had developed. However, if the trade wind speed was high, orographically-
559 forced convection may occur whatever the time of the cycle. The studies of katabatic flow at
560 Guadeloupe (Basse Terre) show that the period from December to March is the most prone to
561 such flows (d'Alexis et al., 2011).

562

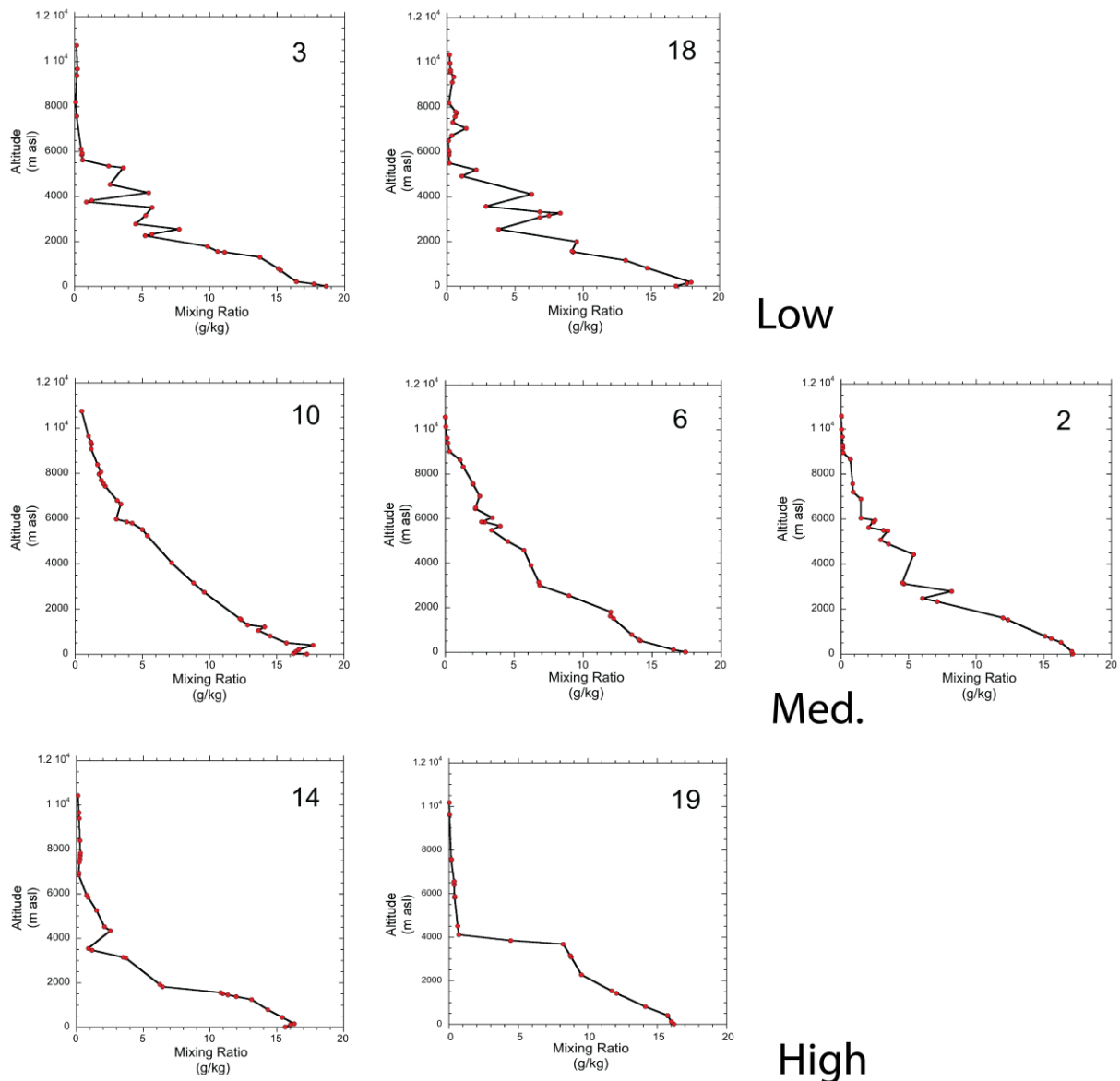
563 **5 Results**

564 5.1 Water vapour fields on individual days

565 Fig.12 shows radiosonde-derived humidity mixing ratio profiles over land (Guadeloupe)
566 measured at 08:00 local time on the days of radar imaging (within two hours of the ascending
567 pass images on 2, 3, 18 and 19 December and within about nine hours of the descending pass
568 images of 6, 10, 14 December). Overall the humidity mixing ratio profiles have mean values in
569 the range 15-16 g/kg between 0 and 0.6 km altitude. The humidity decreases rapidly and
570 smoothly up to altitudes of about 2 km, above which it falls more slowly up to altitudes of 4–9
571 km before dropping to values of < 1 g/kg. The individual humidity profiles tend to have
572 characteristics that match the prevailing wind speed. The profiles of 6 and 10 December are
573 very similar with notably more humidity at higher altitudes (4 – 9 km) than on the other days.
574 Both days have a moderate-wind range. The two low-wind days (3 and 18 December) show
575 very similar profiles with high amplitude inversion structures between 2 and 5.5 km. The two

576 high-wind days (14 and 19 December) also have very similar profiles, falling to very low
 577 humidity values above 4 km. In figure 13 we compare the WMM ZWD fields with the
 578 equivalent ZWD fields derived from GPS at the times of the seven satellite overpasses (Table
 579 1). We can see that the effect of topography in both sets of data is to reduce ZWD value with
 580 elevation at both SHV and Centre Hills (Fig.2c), as we expect. The ranges of ZWD values, due
 581 to topography, calculated by both methods for the seven days give similar average values: $83 \pm$
 582 7 mm for GPS and 79 ± 14 mm for WMM. This suggests that both techniques record similar
 583 gradients of water vapour content.

584



585

586 *Fig.12 Humidity mixing ratio profiles from radiosondes launched at Le Raiset, Guadeloupe at 08:00*
587 *local time on the days of the radar imaging in December labelled in the upper right corner of each*
588 *panel. Profiles are arranged in high-, medium- and low- wind speed rows.*

589

590 The absolute values of ZWD from the WMM simulations are generally higher than those from
591 the GPS method: the difference is least on 18 December (15 mm) and most on 14 December
592 (84 mm). When these differences for each of the seven days are plotted against wind speed
593 (Fig. 13 lower left graph), the difference in ZWD values are shown to diverge with increasing
594 wind speed at a rate of about 11 mm/m/s. This bias associated with wind speed is unexpected.
595 The WMM may be lifting too much water vapour from lower levels during high winds.
596 Alternatively, the bias could represent a faulty assumption of the linearity of the water vapour
597 lapse rate in the GPS-based method, for example, in the un-sampled elevation range between
598 about 600 and 1100 m a.s.l. there is a much higher water vapour content at times of high wind
599 speed than expected from a linear extrapolation from lower elevations.

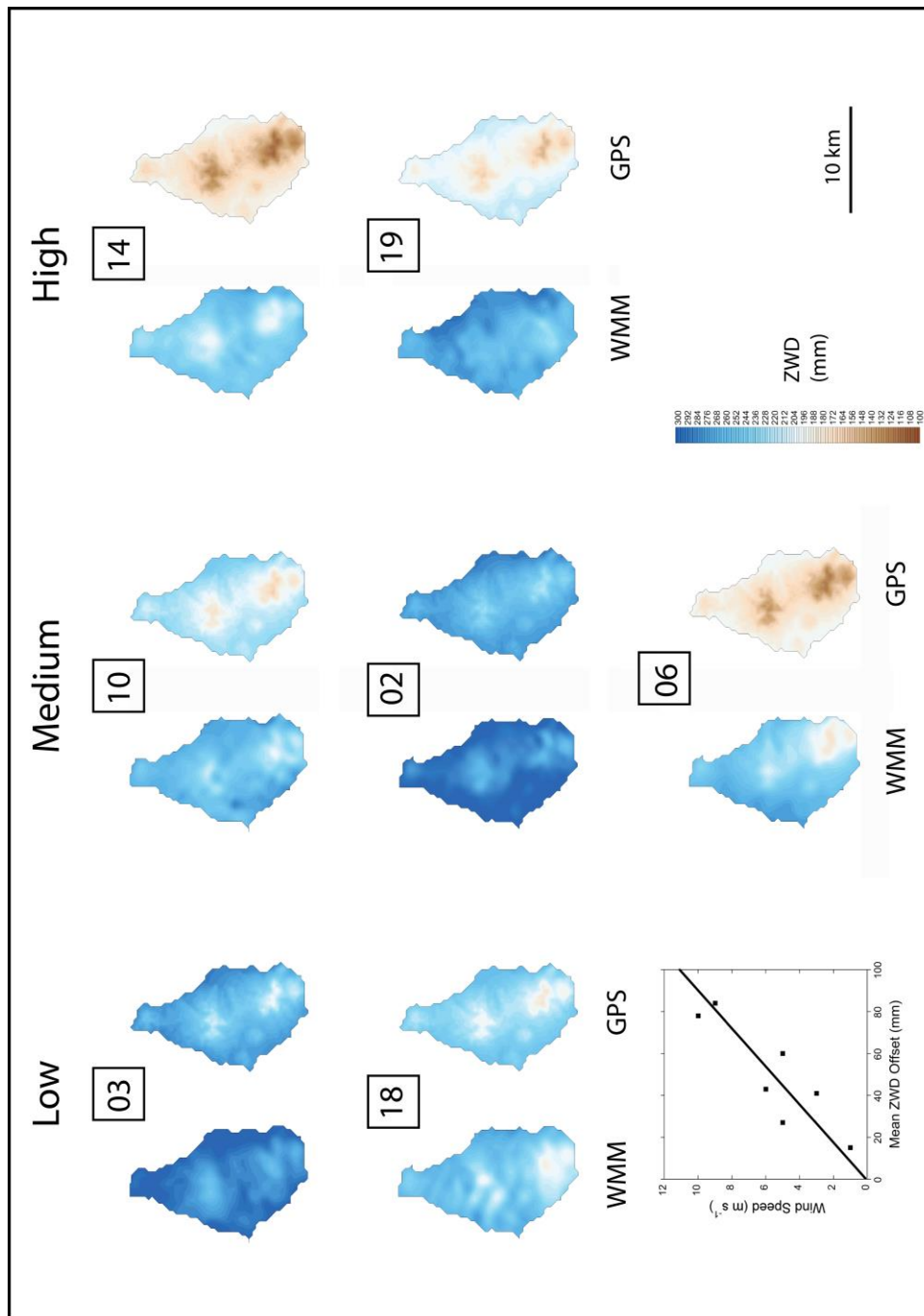
600 The wind on 6 December was from the west (Table 5), as opposed to the usual easterly trade
601 wind direction. In the WMM simulation (Fig. 13) the low levels of ZWD associated with the
602 SHV topography are displaced to the southeastern corner of the island compared to days when
603 the wind was easterly, for example, on 10 December. This is particularly so for the 19 December
604 case, which had high speed, easterly winds and high ZWD values on the southeast, windward
605 coast, equivalent to the high wind-speed case from Dominica illustrated in Fig.8b. Thus, out of
606 the seven cases, the one with clear evidence of reversed trade wind flow (6 December) generates
607 the expected reversal of ZWD asymmetry in the WMM model.

608

609

610

611



613

614

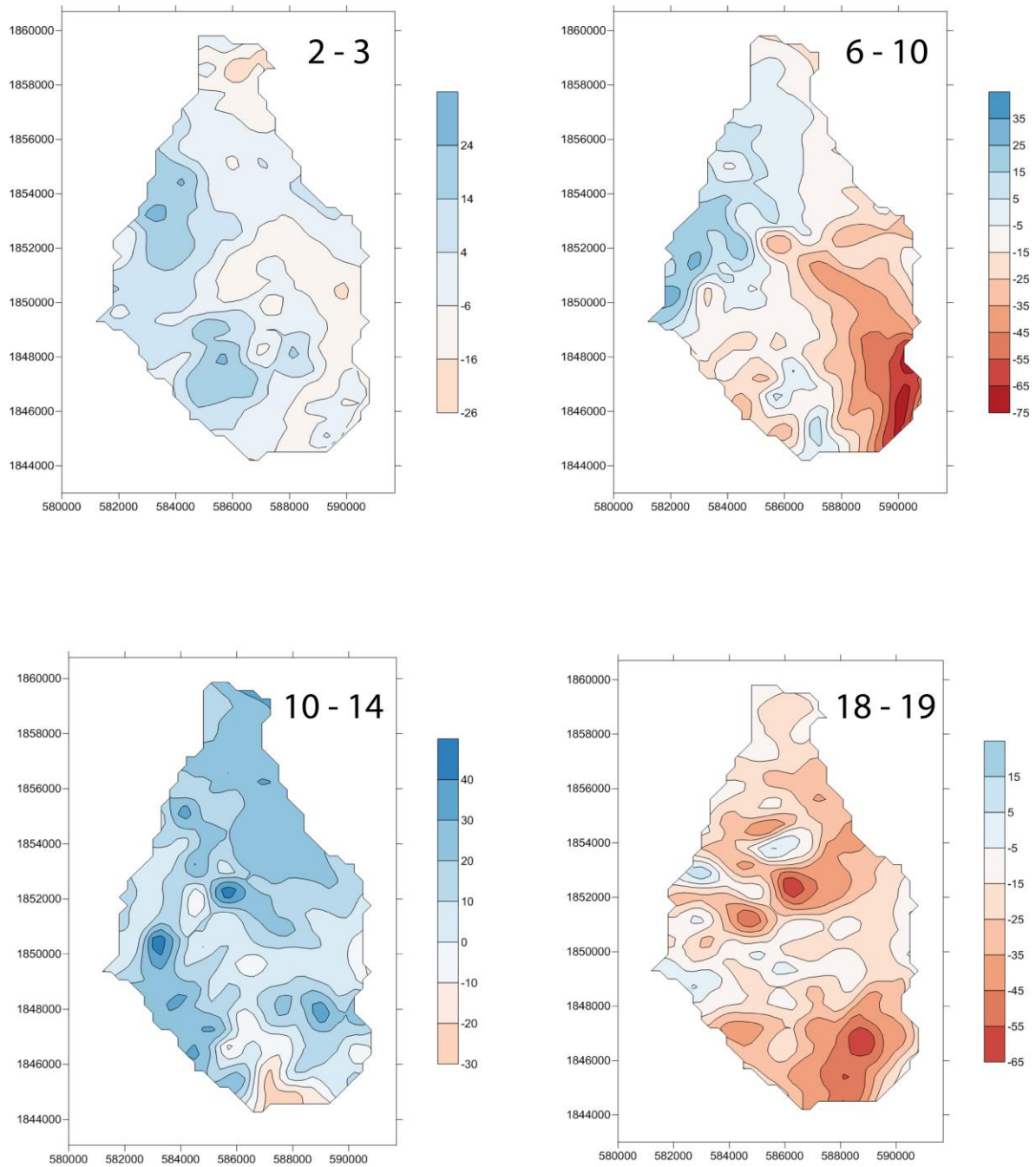
615 *Fig. 13 Pairs of maps of ZWD over Montserrat during December 2014. The date is given by the number*
 616 *between each pair. The left image of each pair is the WMM simulation and the right image is from the*
 617 *GPS method, as described in the text. The pairs are arranged in three columns according to the “low,*
 618 *medium and high” wind speeds on those days (Table 5). The ZWD data are plotted to a horizontal*
 619 *posting of 300 m, the finest model resolution of the WMM. The colour scale of ZWD values shown on*

620 *the bottom row is common to both sets. The graph at the bottom left is of ABL wind speed versus the*
621 *mean offsets in ZWD values between the two methods for the seven days.*

622

623 5.2 WMM differential water vapour fields at zenith

624 The radar image pairs: 2-3, 6-10, 10-14, 18-19 December were chosen for interferogram
625 creation. The WMM-derived maps of ZWD differences (earlier – later) correspond to the four
626 intervals (Fig. 14). Firstly, we compare these ZWD differences with those between the
627 integrated humidity mixing ratios determined by radiosonde profiles between 0 and 2 km a.s.l.
628 (Fig. 12), taken to be representative of the humidity in the ABL. These differential values are:
629 02-03 = +1.4, 06-10 = -3.5, 10-14 = +5.4 and 18-19 = 0.0 g/kg. The positively-valued pairs
630 (02-03 and 10-14) show similarly valued ZWD (Fig.14) whilst the negatively-valued pair (06-
631 10) corresponds to mainly negative ZWD values and the 18-19 pair is dominated by negative
632 ZWD values unlike the radiosonde pair (0 g/kg). Secondly, we assess the spatial patterns of
633 Fig.14. The 2-3 field is of low amplitude with negative values in the east and positive values in
634 the west. A similar pattern is seen in the 6-10 field, except for much larger negative values on
635 the southeast coast. This is the same WMM-derived feature discussed above and as seen in
636 Fig.13 which is probably the result of westerly winds on 6 December and easterly winds on 10
637 December, shifting the low ZWD values above the volcano from the east on the 6 December to
638 the west on the 10 December. The 10-14 field is largely positive, with much more humid values
639 on 10 December. In contrast, the 18-19 field is dominantly negative with generally more humid
640 values on the 19th relative to the 18th. Both the 10-14 and the 18-19 difference fields have most
641 of their variability at the 1 km scale rather than the island-scale patterns of 2-3 and 6-10, perhaps
642 due to model convection noise driven by high wind speed on 14 and 19 September.

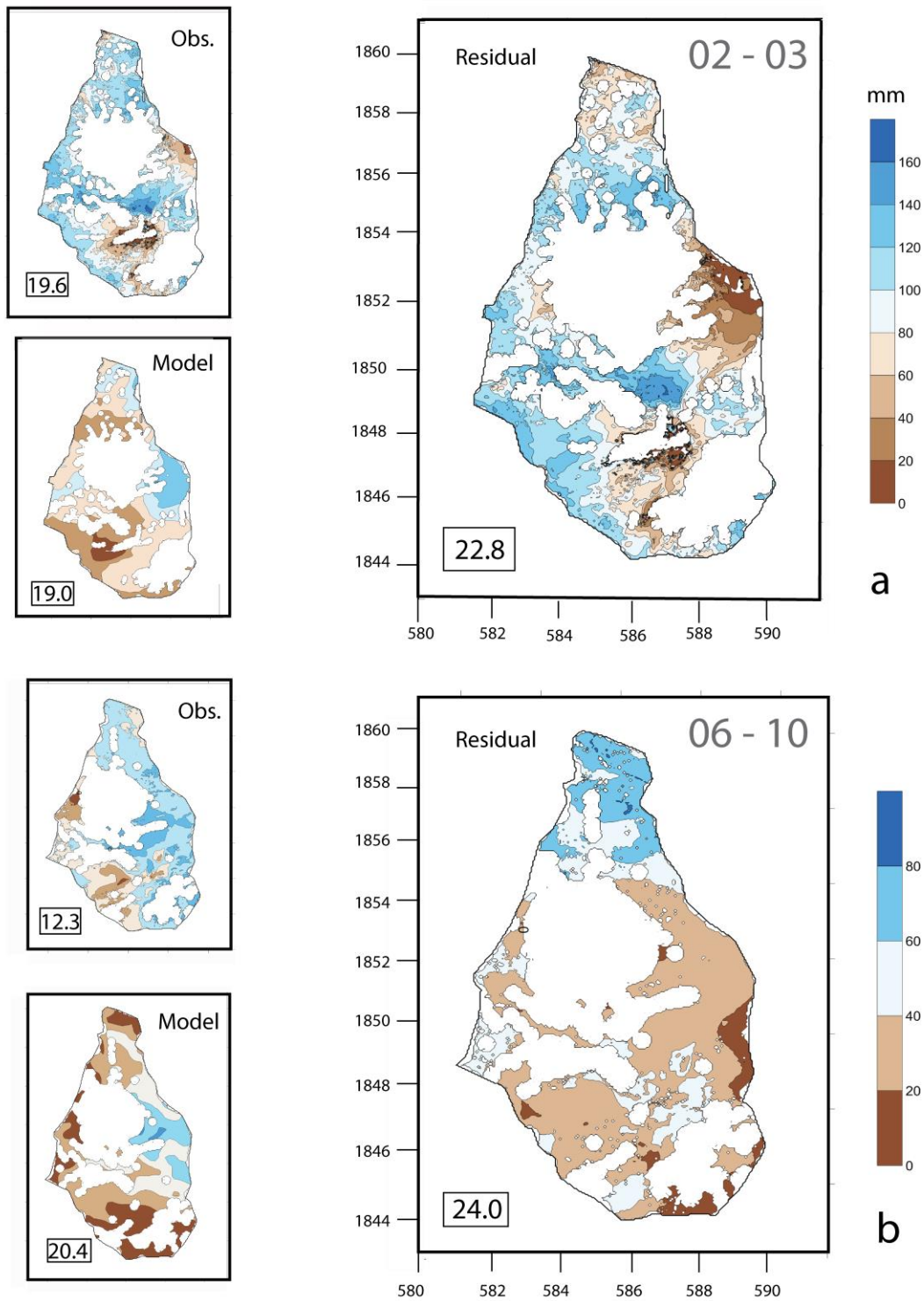


643

644

645 *Fig. 14 WMM-derived ZWD difference fields for four pairs of dates corresponding to the*
 646 *interferograms. Differences in mm (earlier-later). Time intervals in December (days) are given in the*
 647 *top right of each panel. Local grid values in kilometres. Values in lower corner boxes are the rms delay*
 648 *values also shown in Table 6.*

649



650

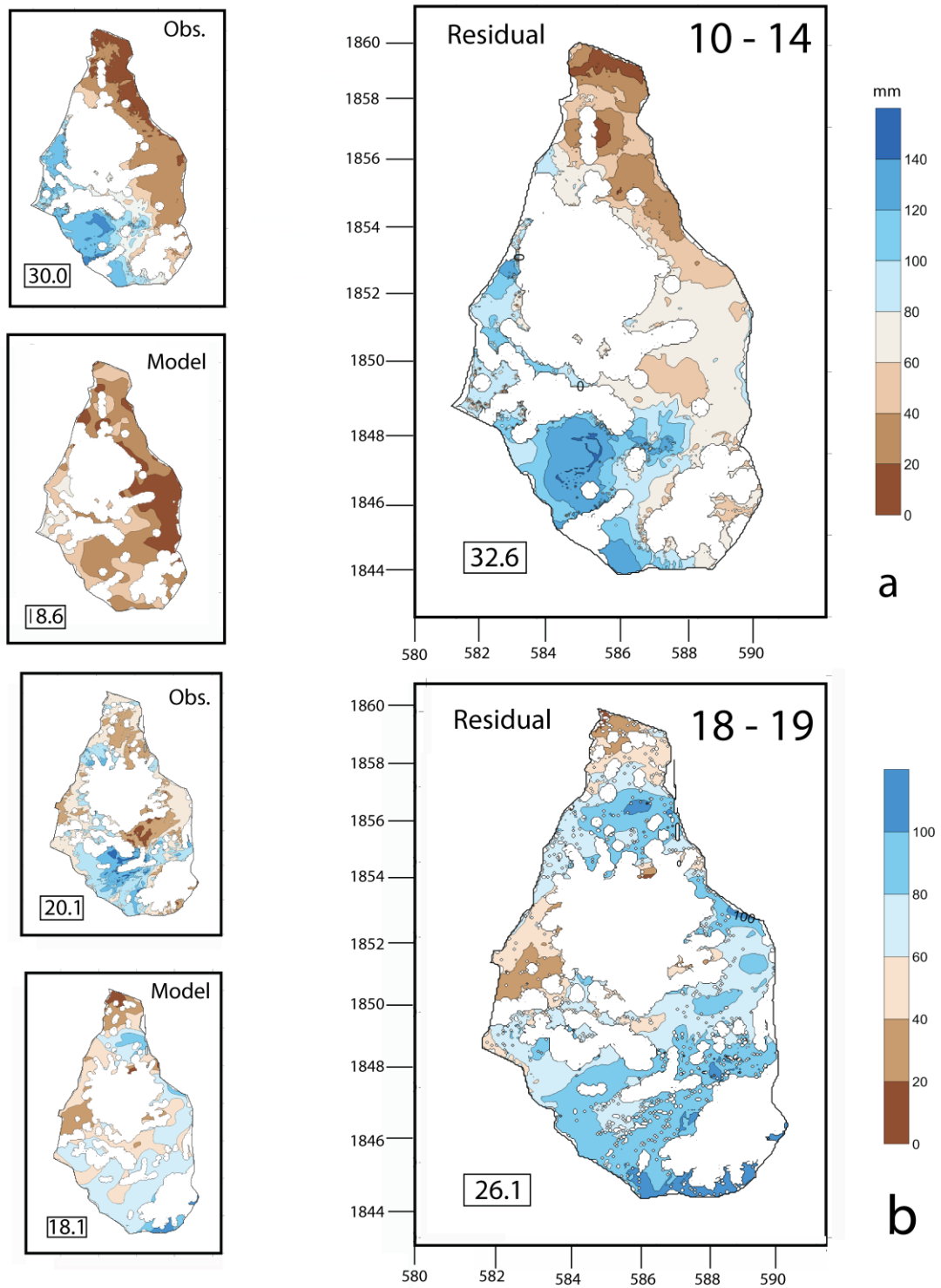
651

652 *Fig.15 Slant wet delay fields for observed (Obs.) interferogram data, modelled (Model) WMM data*

653 *and the Residual (Observed – Modelled) fields for (a) the 2-3 December and (b) the 6-10 December*

654 *intervals. Differences in mm (earlier-later). Local grid values in metres. Values in lower corner boxes*

655 *are the rms delay values also shown in Table 6.*



658 *Fig.16 Slant wet delay fields for observed (Obs.) interferogram data, modelled (Model) WMM data*
 659 *and the Residual (Observed – Modelled) fields for (a) the 10-14 December and (b) the 18-19 December*

660 *intervals. Differences in mm (earlier-later). Local grid values in kilometres. Values in lower corner*
661 *boxes are the rms delay values also shown in Table 6.*

662

663

664 5.4 Differential InSAR - WMM slant fields

665 We now consider the observed delay fields of the COSMO-SkyMed pairs. Specifically, along
666 the slant of the radar paths, 26.6° and 59.2° from zenith. The residual fields created by
667 subtracting the WMM – SWD field from the equivalent field observed by COSMO-SkyMed,
668 including the incoherence masks, are shown in Figs 15, 16. The observed and modelled fields
669 are quite similar for 06-10, 10-14 and 18-19 periods, but not for 02-03.

670

671 2 – 3 December

672 The only obvious feature in common between the observed and modelled delay fields is that
673 the lowest differences are seen around the upper slopes of the volcano. Generally, elsewhere
674 the modelled differences are smaller than the observed differences. The overall range of
675 differences is greatest in this pair of dates.

676

677 6 - 10 December

678 The observed and modelled SWD fields show similar patterns. In the observed field there is a
679 strong gradient across the island with the eastern side of the island having the greatest
680 differences and the south-western side the least change across the two dates. This is also seen
681 in the model results but for a more restricted area on the middle, leeward slopes. The
682 northernmost part of the island shows a contrasting pattern with the highest residuals.

683

684 10 – 14 December

685 The observed SWD field shows a strong gradient of water vapour, high in the southwest, low
686 in the northeast. The modelled version is similar but of a smaller magnitude. The pattern of
687 differences for these 5 days is a reversal of that shown by the 6-10 December interferogram,
688 with a lowest difference on the eastern slopes. This suggests a source that is the common date
689 (10 December) shared by the two intervals. The model field has the smallest range. The
690 humidity mixing ratio is considerably greater on 10 December than on 6 or 14 December
691 (Fig.12), with an inversion horizon 2 km higher than that of 14 December (4 km).

692

693 18 – 19 December

694 On these two days the phase differences were similar in both observed (InSAR) and model,
695 high in the south of the island and low in the north, though the WMM range is generally lower
696 than the InSAR result.

697

698 The range of values in the observed and modelled delay fields is similar, approximately 80-120
699 mm. The two descending pass interferograms (06-10 and 10-14) show strong ENE-WSW
700 gradients across the island (Figs.15, 16) with opposite polarities. The two pairs share the same
701 10 December image, which is the most likely explanation for this pattern. The two ascending
702 pass delay fields (02-03 and 18-19) have shorter intervals (1-day) but less distinct gradients
703 matching the trade wind orientation.

704

705 The WMM model delay fields show some structural similarities to those observed by radar. For
706 example, the 06 -10 WMM field shows higher delay values (more water vapour) in the central
707 windward side of the island, as does the observed field. The WMM field for 18-19 December
708 shows a lower delay value (less water vapour) in the northern half of the island compared to
709 the radar-derived field. The radar fields across the highest parts of SHV tend to show the

710 strongest gradients, suggestive of the abrupt change in flow regime across the island's
 711 topographic divide as shown in Fig.9 b. This is also seen in some of the WMM fields as in 02-
 712 03 and 06-10, but the gradient is less steep.

713

714 The effectiveness of reducing the atmospheric component of phase delay in the interferograms
 715 is assessed by calculating the root mean squared (RMS) error and the percentage of pixel delay
 716 (PPD) between the interferograms and the WRF simulations across the island (Table 6). PPD
 717 is defined here as the pixel-wise offset in the difference field from zero expressed as a
 718 percentage, where 100% would mean a difference field at zero (perfect match) and 0% would
 719 mean all pixels in the difference image would exceed the maximum bounds of the residual
 720 image. We expect a small delay RMS and a high PPD if WRF performs well. The RMS of the
 721 radar interferograms has a mean value of 20.5 mm, less than that of the residual, 26.4 mm Using
 722 the PPD metric the 06-10 value has the most accurate residual of 80.95%, values for 6-10, 10-
 723 14 and 18-19 intervals of 80.9%, 65.42% and 76.82% respectively.

724

725 *Table 6. RMS delay differences for image interferograms with ambient wind speed.*

Dates for each pair	COSMO-SkyMed (mm)	WMM (mm)	Residual (mm)	PPD % (mm)	Average daily wind speed difference (m/s)	Wind comments
2 -3/Dec/2014	19.58	19.01	22.78	64.51	4.8	More E-W flow than S-N
6-10/Dec /2014	12.29	20.41	24.03	80.95	9.5	Strong E-W flow, little S-N flow
10/14/Dec//204	30.05	18.64	32.61	65.42	6.7	Strong S-N flow
18/19/Dec/2014	20.14	18.10	26.06	76.82	2.7	Similar S-N flow to E-W

726

727 Table 7 shows the relative proportions of slant wet delay (SWD), liquid wet delay (LWD) and
 728 hydrostatic delay (HSD) calculated from the WMM difference fields corresponding to the dates

729 of the four interferograms. LWD is calculated using the delay coefficient for cumulus cloud
 730 from Hanssen, (2001), that is the most appropriate (0.7). As expected, SWD is about an order
 731 of magnitude larger than LWD and HSD values. December is just

732

733 *Table 7. Percentage differences of total delay within the WMM apportioned to*

734 *Slant Wet Delay (SWD), Liquid Water Delay (LWD) and Hydrostatic Delay (HSD).*

Dates	SWD %	LWD %	HSD %
2 – 3/Dec/2014	81.9	11.3	6.8
6 – 10/Dec/2014	86.5	9.5	4.0
10 – 14/Dec/2014	88.0	7.1	4.9
18 – 19/Dec/2014	84.7	9.8	5.4

735

736

737 after the end of the wet season in Montserrat (Fig.4). Images of precipitation from the TRMM
 738 satellite show that the only regional rainfall over the period occurred on 6 December during the
 739 passage of a mesoscale feature that skirted Montserrat to the south and also produced westerly
 740 winds. The proportion of LWD (11 - 7 %), generally derived from the WMM, is not negligible.

741

742 **6. Discussion**

743

744 6.1 Understand where and when tropical water vapour originates.

745 The tropics contain the highest levels of atmospheric water vapour as it evaporates above warm
 746 ocean. Our test case SHV volcano, Montserrat lies in the western tropical Atlantic and is subject
 747 to the migration of the ITCZ, northwards during the wet season and southwards in the dry
 748 season. The main effect of the ITCZ is to cycle rainfall and precipitable water vapour, in the
 749 case of Montserrat causing rainfall rates of about 1 mm/day in the dry season to about 5 mm/day
 750 in the wet season. Because of its differential nature, InSAR will tend to give the largest

751 atmospheric signals, with one image from the peak and one from the trough of the ITCZ cycle
752 (e.g. Fig.3). A detailed study of the same effect from Fogo volcano in the eastern tropical
753 Atlantic (Heleno et al., 2010) indicates about 50-30 mm of phase change could be possible at
754 Montserrat, similar to the findings of Wadge et al. (2006). Also the tropical seas of southeast
755 Asia contain a large number of volcanoes, many on islands, that are affected by the ITCZ. The
756 periodicity and amplitude of the ITCZ humidity signal (Martinez et al., 2019; Pausata and
757 Camargo, 2019) are well characterized and hence provide a way to estimate the local scale of
758 water vapour forcing as it affects InSAR on volcanoes.

759

760 6.2 Measure and simulate water vapour over a small mountainous tropical volcano

761

762 There is no easy way to separate the phase delay differences of the two images contributing to
763 the interferogram once its components are combined. Typical ranges of water vapour content
764 variation across Montserrat are about 100 mm. The humidity mixing ratios increase from ~5 -
765 1 g/kg at the top of the ABL (~2 - 4 km altitude) to about 18 g/kg at sea level. (Fig.12)

766 In our experiment we used X-band radar in both ascending and descending paths. The ascending
767 path of the satellites follow an azimuth of 349° at an angle of about 27° to the zenith and the
768 descending path an azimuth of 011° and an angle of about 59° to the zenith. As a result, the
769 length of the descending path through the troposphere is about 1.7 greater than that experienced
770 by the ascending path. The water vapour encountered should be equivalent to this ratio if the
771 path has equivalent specific humidity. The horizontal orientation of the mountain chain forming
772 Montserrat is about 350° , roughly parallel to the ascending radar path, whilst the descending
773 radar path, is oriented about 20° anticlockwise to the topographic axis. The WMM has 5 nested
774 levels, the first 0.3 km grid being the one that just covers Montserrat. Whilst this 300 m scale
775 is adequate for many applications, it is of less value at representing convection simulating

776 clouds, such as the growth of clouds above a heated ground surface (Kirshbaum and Smith,
777 2009).

778

779 6.3 Show how model and observational variations of humid flow depend on the scale and
780 setting of this flow.

781 The direction and speed of the winds, the orientation of the topography, and the diurnal cycle
782 of water vapour are major factors in controlling humid flow. Trade winds blowing from the east
783 dominate in Montserrat. These winds tend to produce asymmetrical humidity fields, with higher
784 values over the windward (eastern) slopes and lower values on the leeward (west) side,
785 particularly when the wind speed is high (>7 m/s). Lee waves tend to form on the leeward side
786 with cloud enhancement and precipitation. At lower wind speeds diurnal solar heating tends to
787 form above hot land surfaces with long trails of clouds converging downwind about 30-40% of
788 the time (Kirshbaum and Fairman, (2015). Out of the 7 days of radar measurements, one (6
789 December) experienced wind from the west (due to a regional system to the southeast). This
790 had a clear impact on the humidity field, creating low specific humidity over the south-eastern
791 flank of the island (Figs. 13,14). The asymmetry of the humidity field during normal trade wind
792 days produces specific humidity values that are greater on the windward relative to the leeward
793 side.

794 Accurate WMM slant delay fields should be identical to those of the contemporaneous
795 interferograms. However, they differ quite significantly as seen in Figs. 15, 16 and Table 6. The
796 standard deviations of the residual images are marginally greater than those of the WMM and
797 InSAR images (Table 6). Spatial offsets of only a few hundred metres in these models are
798 sufficient to generate large local gradients in the humidity fields, e.g. Fig. 16. This misfit has
799 been observed in other interferogram-based studies (e.g. Bekaert et al., 2015). It was thought
800 that the relatively high resolution of the WMM would help mitigate this. But perhaps the 300

801 m horizontal resolution of the model was still too coarse to capture the flow modifying terrain
802 sufficiently well. The lack of detail in the WMM (300 m resolution) is an explanation of why
803 the range of model specific humidity values tend to be less than the InSAR measurements (~2m
804 resolution). In order to capture finer details in the dynamic water vapour profile, alternative
805 approaches, or a hybrid of them, may be adopted such as the use of large-eddy simulation
806 (Kirshbaum and Smith, 2009), statistical models or empirical image processing techniques –
807 although these techniques present their own problems.

808

809

810 **7. Conclusion**

811

812 Unknown amounts of water vapour in the troposphere introduces error in the measurement of
813 geodetic signals, particularly at volcanic islands such as Montserrat. Using InSAR (and GNSS)
814 measurements and WRF modelling, at the time of the overpasses of radar-bearing satellites, we
815 examined the temporal and spatial factors leading to the variability of water vapour. The
816 dominant process that controls the annual water cycle at Montserrat is the ITCZ. This brings an
817 irregular annual dynamic behaviour of water vapour, rainfall and winds. Low values of water
818 vapour occur during the boreal winter and spring and high values in the boreal summer and
819 autumn. The range of specific humidity measured globally by the ITCZ is about 6 g/kg,
820 consistent with that measured locally at Montserrat (and Fogo). Improved knowledge of the
821 ITCZ's climatology and local behaviour would help to forecast water vapour error budgets.

822 Another important factor after water vapour distribution is the trade winds. In the vicinity of
823 the eastern Caribbean the trade winds blow from the east northeast. This is often modified as
824 the ITCZ passes the equator with east southeast flow at higher speeds in summer. Occasionally,
825 the flow is markedly changed or entirely reversed by regional features. This occurred during

826 one day of our experiment (6 December) in which the island-wide wind pattern was reversed.
827 It produced a weak westerly flow and concentration of water vapour in the west, the opposite
828 of the “normal” trade wind pattern.

829 Most days the rising sun coincides with strong surface heating and the ensuing development of
830 both maritime and terrestrial-generated convection. This in turn is susceptible to modification
831 by the local strength of the trade winds and even-more localised convection effects associated
832 with topography. For example, at SHV, several 100 m scale circular refractive phase anomalies
833 are evident as features that wax and wane with the diurnal cycle (Wadge, et al., 2016).

834

835 **Acknowledgements**

836 This work was supported by NERC grant NE/H019928/1 to GW with support from COMET.
837 TW is grateful for the NERC studentship NE/J500082/1. The COSMO-SKYMED radar data
838 were supplied by the Italian Space Agency under a CEOS scheme and we thank M. Pritchard
839 for his help in this regard. We acknowledge the radiosonde data came from the archive of the
840 Department of Atmospheric Sciences, University of Wyoming, the numerical model initial
841 condition data came from the ECMWF, Thomas Christopher at the Montserrat Volcano
842 Observatory provided a climatology dataset and Prof. Daniel Kirshbaum gave access to Fig. 8a.
843 Thanks, also, to Dr. Chris Holloway. The manuscript was greatly improved following
844 comments by four referees and the RSE editing team.

845

846 **References**

847 Alshawaf, F., Hinz, S, Mayer, M., Meyer, F.J. (2015) Construction accurate maps of
848 atmospheric water vapour by combining interferometric synthetic aperture radar and GNSS
849 observations. *J. Geophys Res.*, 120/1391-1403, doi:10.1002/2014JD022419.

850 Barclay, J., Johnstone, J.E., Matthews, A.J. (2006) Meteorological monitoring of an active
851 volcano: implications for eruption prediction. *J. Volcanol., Geotherm. Res.*, 150, 339-358.

852 Bekaert, D.P.S. Hooper, A., Wright, T.J (2015) A spatially variable power law tropospheric
853 correction technique for InSAR data. *J. Geophys. Res.*, 120, 1345-1356, doi:
854 10.1002/2014JB011558.

855 Bekaert, D.P.S. Walters, R.J., Wright, T.J., Parker, D.J. (2015) Statistical comparison of InSAR
856 tropospheric correction techniques, *Rem. Sensing Env.*, 170, 40-47.

857 Bengtsson, L. (2010) The global atmospheric water cycle. *Env. Sci., Lett.*, 5, 025202.

858 Bennitt, G. and Jupp, A. (2012) Operational assimilation of GPS zenith total delay
859 observations into the Met Office Numerical Weather Prediction Models. *Monthly*
860 *Weather Rev.*, 140, 2706-2719.
861
862
863

864 Bevis, M., Businger, S., Herring, T.A., Anthes, R.A., Wadde, R.W. (1994), GPS meteorology:
865 mapping zenith wet delays onto precipitable water. *J. Appl. Meteor.* 33(3), 379-386.

866 Boehm, J., Niell, A., Tregoning, P., Schuh, H., (2006) Global mapping function (GMF): a new
867 empirical mapping function based on numerical weather model data. *Geophys. Res. Lett.*,
868 doi: 10.1029/2005GL025546.

869 Boehm, J. Heinkelmann, R. Schuh, H. (2007) Short Note: A global model of pressure and
870 temperature for geodetic applications. *J. Geod.*, 81, 679-683.

871 Cécé, R., Bernard, D, D'Alexis, C., Dorville, J-F. (2014) Numerical simulations of island-
872 induced circulations and windward katabatic flow over the Guadeloupe Archipelago.
873 *Monthly Weather Rev.*, 142, 850-867.

874 Costantini, M. (1998) A novel phase unwrapping method based on network programming.
875 *IEEE, Trans. Geosci., Rem. Sens.*, 36/3, 813-821.

876 D'Alexis, C., Abouna, A., Berthelot, H., Bernard, D. (2011) Characteristics of nocturnal
877 breezes in the Windward Islands in the southeastern Caribbean: structure and night-time
878 regimes. *J. Caribbean Acad. Sci.*, 5(2).

879 Davison, J.L., Rauber, R.M., Di Girolamo, L., LeMone, M.A. (2013) A revised conceptual
880 model of the tropical marine boundary layer, Part I: statistical characterization of the
881 variability inherent in the wintertime trade wind regime over the western tropical Atlantic.
882 *J. Atmos. Sci.*, 70, 3005-324.

883 Ebmeier, S.K. and co-authors (2018) Synthesis of global satellite observations of magmatic and
884 volcanic deformation: implications for volcano monitoring and the lateral extent of
885 magmatic domains. *J. App. Volcanol.*, 7:2, doi: 10.1186/513617-018-0071-3.

886 Elliott, J.R., Biggs, J., Parsons, B. Wright, T.J. (2008) InSAR slip rate determination on the
887
888 Altyn Tagh Fault, northern Tibet, in the presence of topographically correlated
889
890 atmospheric delays. *Geophys. Res. Lett.*, 35, L12309, doi:
891
892 10.1029/2008GL033659
893

894 Fattahi, H., Amelung, F. (2014) Insar uncertainty due to orbital errors. *Geophys. J. Int.*, 199/1,
895 549-560.

896 Fattahi, H., Simons, M., Agram, P., (2017) InSAR time-series estimation of the ionospheric
897 phase delay: an extension of the split range-spectrum technique., *IEEE, Trans., Geosci, Rem,*
898 *Sens.*, 55/10, doi: 10.1109/TGRS.2017.2718566.

899 Hanssen, R.F. (2001) *Radar Interferometry. Data interpretation and error analysis.* Kluwer
900 Academic Publishers,, Dordrecht, 308 pp.

901 Feng, J., Zhen, W., Wu, Z. (2017) Ionospheric effects on repeat-pass SAR interferometry. *Adv.*
902 *Space Res.*, 60, 1504-1515, doi: 10.1016/j.asr.2017.06.019.

903 Herring, T.A., King, R.W., Floyd, M.A. and McClusky, S.C. (2010a) GAMIT Reference
904 Manual, GPS Analysis at MIT. *Department of Earth, Atmospheric and Planetary Sciences,*
905 *Massachusetts Institute of Technology, Cambridge, USA.*

906 Herring, T. A., Floyd, M.A., King, R. W., and McClusky, S. C. (2010b) GLOBK reference
907 manual, Global Kalman filter VLBI and GPS analysis program. *Department of Earth,*
908 *Atmospheric, and Planetary Sciences, Massachusetts Institute of Technology, Cambridge.*
909 *USA.*

910 Hofmann-Wellenhof, B., Lichtenegger, H., Collins, J. (1995) Global Positioning System,
911 Theory and Practice, 3rd edition, Springer-Verlag, Wien.

912 Goldstein, R.M. and Werner, C.L. (1998) Radar interferogram filtering for geophysical
913 applications. *Geophys., Res., Lett.*, 25/21, 4035-4038,10.1029/95GL900033.

914 Gonzalez, A., Exposito, F.I., Perez, J.C., Diaz, J.P., Taima, D. (2013) Verification of
915 precipitable water vapour in high resolution WRF simulations over a mountainous
916 archipelago. *Q. J. R. Meteorol., Soc.*, 139:2119-2133.

917 Heleno, S.I.N., Frischknecht, C., d'Oreye, N., Lima, J.N.P., Faria, B., Waff, R., Kervyn, F.
918 (2010) Seasonal tropospheric influence on SAR interferograms near the ITCZ- the case of
919 Fogo Volcano and Mount Cameroon. *J. African Earth Sci.*, 58/5 833-856. 10.1016/j-
920 jafreasci, 2009-07-013.

921 Li, Z., Fielding, E., Cross, P., Muller, J-P., (2005) InSAR atmospheric correction – GPS
922 topography-dependent turbulence model (GTTM). *J. Geophys. Res.*, 110, B02404, doi:
923 10.1029/2005JB003711.

924 Li, Z., Cao, Y., Wei, J., Duan, M., Wu, L., Hou, J., Zhu, J., (2019) Time series InSAR ground
925 deformation monitoring: atmospheric delay modelling and estimating. *Earth Sci. Rev.*, 192,
926 258-284.

927 Jolivet, R., Grandin, R., Lasserre, C., Doin, M-P., Peltzer, G., (2011) Systematic InSAR
928 tropospheric phase delay corrections from global meteorological reanalysis data. *Geophys.,*
929 *Res., Lett.*, 38, L17311 doi: 10.1029/2011GL 048757.

930 Jolivet, R., Agram, P.S., Lin, N.Y., Simons, M., Doin, M.P., Peltzer, G., Li, Z. (2014)
931 Improving InSAR geodesy using global atmospheric models. *J. Geophys., Res.*, 119(3),
932 2324-2341.

933 Kirshbaum, D.J., Durran, D.R. (2004) Factors governing cellular convection in orographic
934 precipitation. *J. Atmos. Sci.*, 61, 682-698.

935 Kirshbaum, D.J., Smith, R.B. (2009) Orographic precipitation in the tropics: large-eddy
936 simulations and theory. *J. Atmos. Sci.*, 66, 2559-2578.

937 Kirshbaum, D.J., Fairman Jr., J.G. (2015) Cloud trails past the Lesser Antilles. *Monthly*
938 *Weather Rev.*, April 2015, 995-1017.

939 Kirshbaum, D. J., (2017) On upstream blocking over heated mountain ridges. *Q. J. R.*
940 *Meteorol. Soc.*, 143: 53-68.

941 Laderach, A., Raible, C.C., (2013) Lower troposphere humidity: climatology, trends and the
942 relation to the ITCZ. *Tellus A*, 65, 20413, doi10.3402/tellus v.6510.20413.

943 Lager K., Schindelegger M., Bohm J., Krasna H., Nilsson T (2013) GPT2: Empirical slant delay
944 model for radio space geodetic techniques. *Geophys. Res. Lett.* 40,6, 1069-1073.

945 Lu, Z., Dzurisin, D. (2014) *InSAR imaging of Aleutian Volcanoes*, Springer, New York, pp.390.

946 McVicar, T.R. and Korner, C. (2013) On the use of elevation, altitude and height in the
947 ecological and climatological literature. *Oecologia*, 171, 335-357. Doi: 10.1007/S00442 –
948 012-2416-7.

949 Massonnet, D. and Feigl, K. (1998) Radar interferometry and its application to changes in the
950 Earth's surface. *Rev. Geophys.*, 36, 441-500.

951 Matthews, A.J., Barclay, J., Carn, S., Thompson, G., Alexander, J., Herd, R.A., Williams, C.
952 (2002) Rainfall-induced volcanic activity on Montserrat. *Geophys. Res. Lett.*, 29, (130),
953 1644, doi:10.1029/2002GL014863.

954 Martinez, C., Goddard, L., Kushnir, Y., Ting, M. (2019) Seasonal climatology and dynamical
955 mechanisms of rainfall in the Caribbean. *Climate Dynamics*, doi: 10.1007/s00382-019-
956 04616-4.

957 Minder, J.R., Smith, R.B., Nugent A.D. (2013) The dynamics of ascent-forced orographic
958 convection in the tropics: results from Dominica. *J. Atmos. Sci.*, 70, 4067-4088.

959 Munoz, E., Busalacchi, A.J., Nigam, S., Ruiz-Barradas, A. (2008) Winter and summer structure
960 of the Caribbean Low-Level Jet., *J. Climate*, 21/1260-1276.

961 Nugent, A.D., Smith, R.B., Minder, J.R. (2014) Wind speed control of tropical orographic
962 convection. *J. Atmos. Sci.*, 71, 2695-2712.

963 Odbert, H.M., Ryan, G.A., Mattioli, G.S., Hautmann, S., Gottsmann, J., Fournier, M., Herd,
964 R.A., (2014) Volcanic geodesy at Soufriere Hills Volcano, Montserrat: a review. From:
965 Wadge, G., Robertson, R.E.A., Voight, B. (eds.) The eruption of Soufriere Hills Volcano,
966 Montserrat from 2000 to 2010. Geol. Soc. London, Memoirs, 39, 195-217.
967 doi/10.1144/M39.11.

968 Pausato, F.S.R., Camargo, S.J. (2019) Tropical cyclone activity affected by volcanically
969 induced ITCZ shifts. *PNAS*, 116/16 , doi:10.1073/pnas.1900777116.

970 Poulidis, A.P., Renfrew, I.A., Matthews, A.J. (2016) Thermally induced convective circulation
971 and precipitation over an isolated volcano. *J. Atmos. Sci.*, April 2016. Doi: 10.1175/JAS-D-
972 14-0327.1.

973 Pritchard, M. E. and co-authors (2018) Towards coordinated regional multi-satellite InSAR
974 volcano observations: results from Latin America pilot project. *J. App. Volcanol.*, 7:5
975 doi/10.1186/513617-018-00746.

976 Richter, I., Xie, S-P., Morioka, Y., Doi, T., Taguchi, B., Behera, S., (2017). Phase locking of
977 equatorial Atlantic variability through seasonal migration of the ITCZ. *Clim. Dyn.*, 48, 3615-
978 3289.

979 Siebsma, A.P., Bretherton, C.S., Brown, A., Chlond, A., Cuxart, J., Duynkerke, P.G., Jiang, H.,
980 Khairoutdinov, M., Lewellen, D., Moeng, C-H, Sanchez, E., Stevens, B., Stevens, D.E.
981 (2003) A large eddy simulation inter-comparison study of the shallow cumulus convection.
982 *J. Atmos. Sci.*, 60/10, 1201-1219.

983 Schneider, T., Bischoff, T., Haug, G.H. (2014) Migrations and dynamics of the Intertropical
984 Convergence Zone. *Nature, Review*.513, 45-53.

985 Skamarok, W.C., and co-authors (2008) A description of the Advanced Research WRF version
986 3. *NCAR Tech. Note NCAR/TN-475+STR*, 113 pp.

987 Smith, R.B., Gleason, A.C., Gluhosky, P.A., Grubisic, V. (1997) The wake of St Vincent. *J.*
988 *Atmos. Sci.*, 54, 606-623.

989 Smith, R.B., Minder, J.R., Nugent, A.D., Storelvmo, T., Kirshbaum, D.J., Warren, R., Lareau,
990 N., Palany, P., Arlangton, J., French, J. (2012) Orographic precipitation in the tropics. *Bull.*
991 *Am. Meteor. Soc.*, October, 2012,1567-1579.

992 Spaans, K., Hooper, A., (2016) InSAR processing for volcano monitoring and other near real-
993 time applications. *J. Geophys. Res.: Solid Earth*, 121,2947-2960. 10.1002/2015JB012752.

994 Stevens, B., (2006) Bulk boundary-layer concepts for simplified models of tropical dynamics.
995 *Theor. Comput. Fluid Dyn.* 20, 279-304.

996 Stinton A., Bass V., Christopher T., Edgecombe N., Fergus M., Pascal K., Smith P., Stewart
997 R., Syers R., Williams C. (2016) MVO Scientific Report for Volcanic Activity between 1
998 October 2015 and 30 April 2016, *Montserrat Volcano Observatory Open File Report OFR*
999 *16-02*.

1000 Stull, R.B., (1988) *An introduction to boundary layer meteorology*. Springer, Heidelberg, 666
1001 pp.

1002 Taylor, M.A., Alfaro, E.J. (2005) Climate of Central America and the Caribbean. In: *Oliver*
1003 *J.E., Encyclopedia of World Climatology*. Encyclopedia of Earth Sciences series. Springer,
1004 Dordrecht.

1005 Wadge, G., Webley, P.W., James, I.N., Bingley, R., Dodson, A., Waugh, S., Veneboer, T.,
1006 Puglisi, G., Mattia, M., Baker, D., Edwards, S.C., Edwards, S.J., Clarke, P.J. (2002)
1007 Atmospheric models, GPS and InSAR measurements of the tropospheric water vapour field
1008 over Mount Etna. *Geophys. Res. Lett.*, 29/19, 11-1 - 11-4, doi: 10.1029/2002GL015159.

1009 Wadge, G., Mattioli, G.S., Herd, R.A. (2006) Ground deformation at Soufriere Hills Volcano,
1010 Montserrat during 1998-2000 measured by radar interferometry and GPS. *J. Volcanol.*
1011 *Geotherm. Res.*, 152/1-2, j.jvolgeores,205.11.007.

1012 Wadge, G., Zhu, M., Holley, R.J., James, I.N., Clark, P.A., Wang, C., Woodage, M.J. (2010)
1013 Correction of atmospheric delay effects in radar interferometry using a nested mesoscale
1014 atmospheric model. *J. App. Geophys.*, 72, 141-149.

1015 Wadge, G., Voight, B., Sparks, R.S.J., Cole, P.D., Loughlin, S.C., Roberston, R.E.A., An
1016 overview of the eruption of Soufriere Hills Volcano from 2000 to 2010. From: Wadge, G.,
1017 Robertson, R.E.A., Voight, B. (eds.) *The eruption of Soufriere Hills Volcano, Montserrat*
1018 *from 2000 to 2010*. Geol. Soc. London, Memoirs, 39, 1-39. doi/101144/M39.11.

1019 Wadge, G., Costa, A., Pascal., K., Werner, C., Webb, T. (2016) The variability of refractivity
1020 in the atmospheric boundary layer of a tropical island measured by ground-based
1021 interferometric radar. *Bound. Layer Meteorol.* 161/2, 309-333. doi:10.1007/s10546-016-
1022 0168-3.

1023 Waliser, D. E., Gautier, C. (1993) A satellite-derived climatology of the ITCZ. *J. Climate*, 6,
1024 2162-2174

- 1025 Wang, C-C., Kirshbaum., D.J. (2015) Thermally forced convection over a mountainous tropical
1026 island. *J. Atmos. Sci.*, 72, 2484-2506.
- 1027 Webb, T.L. (2015) High resolution atmospheric modelling of a tropical island for space
1028 geodesy. *Ph.D. thesis, University of Reading.*
- 1029 Zebker H.A., Villasenor, J. (1992) Decorrelation in interferometric maps. *IEEE Trans. Geosci.,*
1030 *Rem. Sensing*, 30/5, 950-959.

1032 *Supplement 1*

1033

1034 **Method to simulate the ZWD field from GPS-derived values**

1035

1036

1037 In practice, we use a 4-step method to separate and interpolate the topographic and dynamic
1038 components of the zenith wet delay field before recombining them:

1039

1040 1. Normalize the ZWD values to sea-level equivalence for all 14 sites using the ZWD lapse
1041 rate. Assume that the remaining anomalies are due to horizontal differences in the water
1042 vapour field.

1043

1044 2. Interpolate the 14 (or less, depending on receiver availability) values of lateral delay to a 25
1045 m grid using kriging to create field H.

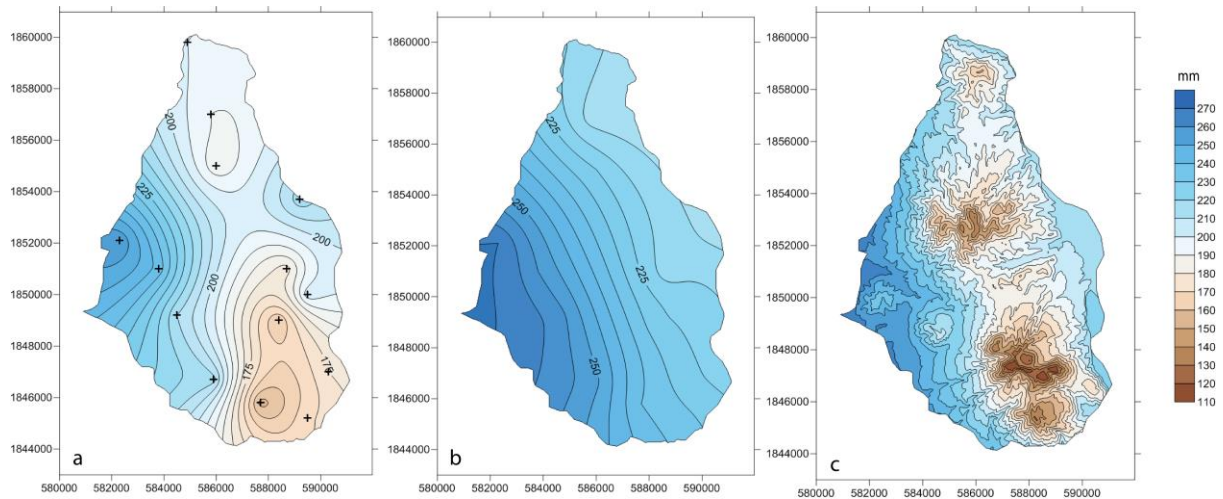
1046

1047 3. Multiply the elevation values at each 25 m posting of the DEM (equivalent to field H) with
1048 the ZWD lapse rate. This gives the vertical variability due to topography, field V.

1049

1050 4. Add fields H (horizontal component) and V (vertical component).

1051



1052

1053

1054 *Fig. S1 ZWD fields (mm) at 17:30 (local time) on 3rd August 2013. (a) Field interpolated from the 14 GPS*
 1055 *observation sites (black crosses). (b) Horizontal gradient field after normalising values in (a) to sea level. (c)*
 1056 *Combined horizontal (b) and vertical fields interpolated using the water vapour lapse rate (0.14 mm/m) multiplied*
 1057 *by the elevations of each cell of a 25 m horizontal resolution DEM.*

1058

1059 Figure S1 shows the resulting ZWD field for the 17:30, 3rd August 2013. Low values of ZWD
 1060 are concentrated along the central, mountainous, spine of the island (Fig. S1a). But the lack of
 1061 observations in the central part of the island produces higher than expected values in the
 1062 interpolated field. The horizontal component of the field shows a clear ENE gradient of about
 1063 50 mm of delay across the island (Fig. S1b). This gradient is the same orientation as that
 1064 observed by MODIS and WMM (Fig. 4), and is of similar amplitude compared to the lee wave
 1065 anomalies from WMM of ~70 mm. The full, 25m horizontal resolution ZWD field is shown in
 1066 Fig. S1c.